Passive Autonomy: Hygromorphic Rotational Actuators

Design & Evaluation

Sebastiaan Theodoor Joosten

Passive Autonomy: Hygroscopic Rotational Actuators Design & Evaluation Sebastiaan Theodoor Joosten

TU Delft

Passive Autonomy: Hygromorphic Rotational Actuators

Design & Evaluation

by

Sebastiaan Theodoor Joosten

to obtain the degree of Master of Science
at the Delft University of Technology,
to be defended publicly on Thursday August 6, 2020 at 14:00.

Student number:	4103513	
Project duration:	September 1, 2019 – August 6, 2020	
Thesis committee:	Prof. dr.-ing. H. Vallery,	TU Delft, supervisor
	Dr. ir. G. Radaelli,	TU Delft
	Dr. Mohammad J. Mirzaali,	TU Delft

TU Delft

Preface

I have always been fascinated by the natural world around us. My first answer to the question 'what do you want to be when you grow up' was 'Biologist!', uttered whilst sitting in the middle of an anthill. As time progressed, I got more and more interested in the human world, with all its intriguing mechanisms and technologies. My interest in nature kept lingering in the background, however. When Giuseppe introduced me to the concept of mechanisms that exhibit their movement by large deformations over an entire surface (compliant shell mechanisms) my interest was piqued immediately. Something that is both functional and beautiful, it reminded me of nature. And indeed, while compliant shells are relatively new in the human world, plants have been using them for a long time. I was sure they could teach us engineers a thing or two!
I am very happy to bring everything full circle by presenting to you this thesis, covering the subject of a compliant shell mechanism that, inspired by working principles from the plant world, autonomously rotates when exposed to water. I hope you have as much fun reading about these phenomena as I had (re)discovering them.

Sebastiaan Theodoor Joosten
Delft, July 2020

Contents

1 Introduction

While mechanisms that move through deformation of large thin-walled structures , i.e. compliant shell mechanisms, are relatively new in the engineering world, plants have been incorporating this principle since before humans walked the earth. As a result, many interesting compliant shell mechanisms exist in the plant world that can be of inspiration for engineers and designers [3, 5].

Plants have developed smart ways of moving without the need of an internal initial stimulus or providing energy [1, 5]. Most notable is the use of structures that swell or shrink based on water uptake, a process called hygroscopy [6]. Many interesting spatially curved moving surfaces arise from this simple principle.

Principles of the plant world are being used for design purposes more and more [12, 14, 15]. A relatively new body of work, hygromorphic actuators [7], initiate their movement independent of human intervention and deform without the need of an energy supply. These passive autonomous actuators show promising results, but more variety in the possible motions that can be achieved is desirable [3, 21].

This thesis discusses the design of a hygromorphic compliant shell that shows a rotational deformation as humidity increases. This Hygromorphic Rotational Actuator (HRA) is a unique addition to the library of hygromorphic actuators.

1.1. Objectives

- Design a compliant shell that rotates when exposed to water
- Investigate the influence of the dimensional parameters on the angular deformation and torque

1.2. Thesis Outline

The main body of this thesis is the paper contained in chapter 2. The conceptual design of the HRA is presented here, along with its embodiment, performance analysis and prototype experiments. Chapter 3 and 4 will discuss some additional interesting aspects of the HRA that were not developed enough or would distract from the paper, but are worth mentioning nonetheless. The appendix that follows contains more detailed information about the fabrication of the HRA prototype (A) and its material properties (B), a full description of the test set-up (C), a guide of the steps taken during the numerical simulations (D) and some supplementary info (E).

2

Passive Autonomy: Hygromorphic Rotational Actuators

Passive Autonomy: Hygromorphic Rotational Actuators

Sebastiaan Joosten, Giuseppe Radaelli, and Heike Vallery

***Abstract*—Inspired by phenomena in the plant world, a meteoro-sensitive rotational actuator is developed. The design uses a hygro-active shell, whose water-based swelling is restricted at selective locations to form a helicoid structure. The influence of geometrical parameters on the performance is investigated using a numerical analysis of various geometries, by looking at resulting rotation and torque during this rotation. Prototypes are built of five key geometries in the design space, to validate the simulations and to investigate the real-life behaviour of the design. These prototypes are submerged in water to investigate their deformation, after which they are placed in a torsion machine to investigate the torque during rotation. The experiments result in similar rotations and torques as the simulations. The designed Hygromorphic Rotational Actuator is capable of passively rotating its own structure, thereby expanding the possibilities of engineers and designers when designing passive autonomous systems.**

I. Introduction

In engineering, swelling and shrinking of a material in response to absorbing or desorbing water is generally something to avoid. Plants, however, often use this phenomenon to their advantage [1]–[3].

Hygroscopy is frequently used by plants as basic movement initiator to create a passive motion. Fibrous tissue swells because it equilibrates its water content with the ambient humidity [4]. This swelling is selectively resisted to amplify the movement [5], for instance by a layer of non-hygroscopic material. The resulting bilayer structure will bend when exposed to water [6]. Well-known examples are the opening of seedpods such as pinecones [7] or the movement of wheat awns [2].

Other amplification mechanisms plants use to amplify a basic movement initiator, are based upon what humans would call failure mechanisms. Various seed catapults rely on fracture to release stored energy, shooting their seeds away [1], [8]. Flower opening often relies on differential elongation of the edge with respect to the midrib, causing a snap-through buckling [9], [10].

The combination of water-driven swelling or shrinking of structures with a selective restriction of this swelling or shrinking enables the autonomous movement of plant structures without costing energy. Sensing, actuating and moving happens within the same structure, saving space and increasing efficiency [5], [11].

In some disciplines, methodologies are developed to incorporate natural working principles in the design process [12], [13]. Engineers and designers are gradually adopting these hygromorphic shell structures in their designs [14]–[16]. Most notably, hygro-active building envelopes are being developed to passively regulate the shading and ventilation of buildings, in response to the surrounding humidity [17]–[19]. Hygromorphic bilayers are even being used for the locomotion of small hygro-active robots [20].

These examples show that passive hygromorphic actuators can benefit various engineering fields. They move completely autonomous based on environmental stimuli and do not require a supply of energy, making them suitable for interesting applications. However, the majority of existing hygromorphic shell actuators are based on bending or translation [3], [14]–[16], [21]. Although some twisting hygro-active structures have been developed, they are built out of composite multi-layer segments that deform simultaneously and as a result their rotation can not be precisely controlled [22].

In order to expand and improve the possibilities of these passive autonomous structures, this research focusses on the development of a hygroscopic shell that rotates with increasing environmental humidity. Its rotation can be controlled by careful selection of the main dimensional parameters.

Two working principles found in the plant world are combined. Hygroscopic swelling is used as a basic movement initiator to start the motion. Selective restriction of this translational swelling is used to cause differential edge elongation. This elongation serves as the amplification mechanism, which transfers the small swelling to a larger rotation.

The design is analysed by building a FEM-model based on a custom Isogeometric Analysis package (IGA). The influence of the main geometrical parameters on the resulting rotation and torque is investigated. Finally, a set of prototypes is fabricated to experiment with the real-life behaviour of the design and to verify the simulated model.

II. Methods

A. Conceptual Design

To generate a hygromorphic rotation with a shell structure, two of the aforementioned working principles from the plant world are combined (see figure 1). The presented Hygrmorphic Rotational Actuator (HRA) consists of a rectangular sheet of orthotropic hygroscopic material. When exposed to water, this material only extends in the vertical direction. A well-known example of such a material is wood [23].

This hygroscopic expansion is selectively resisted by applying constraints. While in a bilayer system the constraint consists of a complete second non-hygro-responsive shell attached to the first one [2], here only a constraint restricting expansion across the vertical centreline of the shell is applied. Furthermore, both the top and bottom horizontal edges are forced to keep a 90 degree angle with this centreline. Their movement is still allowed in the xy-plane. See figure 2a for a schematic of the constraints implemented in the design.

These selective restrictions impose a gradient on the amount of vertical elongation that is possible, being zero at the shell centre and increasing towards the shell edges. While this

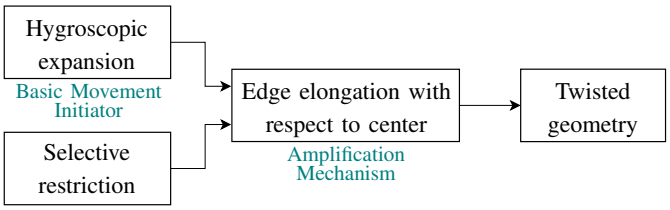

Figure 1: Schematic of events leading to the movement of the HRA. The hygroscopic expansion of the shell in vertical direction is selectively restricted on the vertical centreline, thereby forcing the edges to become longer than the centre. This causes the top and bottom edge to rotate with respect to one another, twisting the geometry. The constraints and the deformation they cause are also depicted in figure 2.

edge elongation causes a snap-through buckling with the petals of a lily [9], here it forces the shell to twist into a helicoid shape due to the 90 degree angle constraint. It thereby rotates the top and bottom edges with respect to each other, while staying parallel to the xy-plane (see figure 2b).

B. Analytical model of geometrical parameters

In the deformed state, the surface will take on a shape resembling a helicoid. With a known hygroscopic expansion, the theoretical achievable angle can be determined based on the main geometrical parameters r (radius, measured from shell centreline to shell edge) and h (height of shell, measured across its centreline) by looking at the length of the edge L_e of the surface.

In figure 3, a helical curve is projected onto a cylindrical surface. This surface is then cut with this helical line and rolled out flat, so that a triangular shape is formed [24]. The length of this helix is defined by the height of the cylinder and the amount of circumferences the helix completes, using Pythagorean theorem.

$$L_i = \sqrt{h^2 + C_i^2} = \sqrt{h^2 + (2\pi i)^2 \cdot r^2}, \tag{1}$$

where h is the height of the cylinder, $C_i = 2\pi i \cdot r$ is the travelled distance in terms of a fraction i of the circumference, r is the radius of the base circle and L_i is the length of the helix.

The movement of the presented design is driven by edge elongation and has rotation as the dependent variable. This elongation is caused by the hygroscopic strain of the material in vertical direction. Since the original geometry is a rectangular shell with vertical edges of equal length, the new length of the outer edge L_e after deformation is

$$L_\mathrm{e} = h \cdot (1 + S_\mathrm{h}), \tag{2}$$

where S_h is the engineering strain caused by hygroscopic swelling.

Substituting equation 2 into equation 1 and rearranging terms to obtain the relation for an arbitrary rotation yields

$$h \cdot (1 + S_\mathrm{h}) = \sqrt{h^2 + (2\pi i)^2 \cdot r^2}, \tag{3}$$

$$2\pi i = \sqrt{\frac{(h \cdot (1 + S_\mathrm{h}))^2 - h^2}{r^2}}. \tag{4}$$

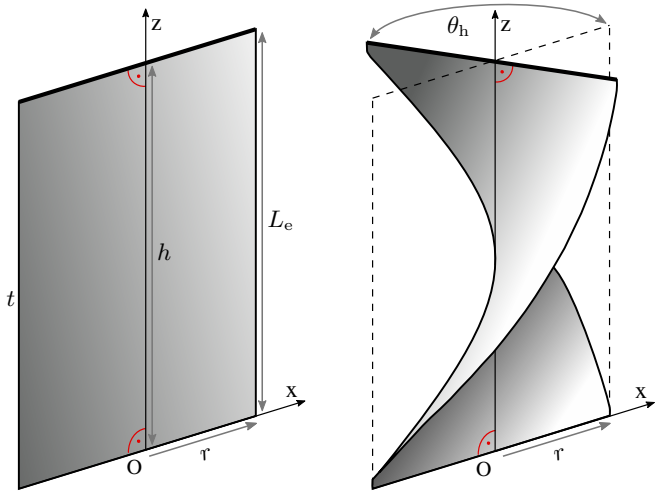

(a) Schematic of the HRA in undeformed state.

(b) Schematic of the HRA in deformed state, after being exposed to water.

Figure 2: Schematic of the HRA, before (a) and after (b) being exposed to water. Radius r, height h and thickness t are the main geometric parameters that are being investigated. θ is the resulting angle. The movement is based on the differential elongation of the vertical edge L_e with respect to the length of the vertical centre h. The top and bottom horizontal edges are rigid and are forced to maintain a 90 degree angle with the vertical centreline.

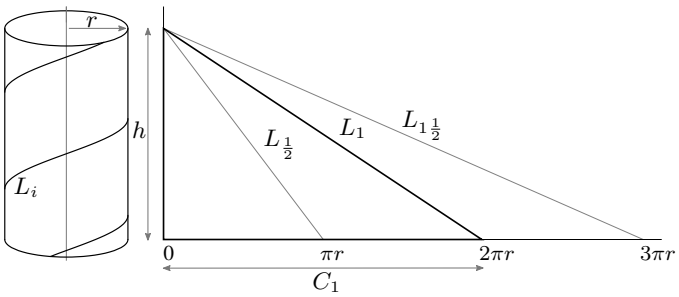

Figure 3: Schematic of dimensional properties of a rolled-out helix. The length L_i of the helix is defined by the height h of the cylinder that it envelops and the amount of circumferences $C_i = 2\pi i \cdot r$ it completes.

This result can then be generalised to provide the angular rotation in degrees for each set of S_h, h and r:

$$\theta_\mathrm{h} = \frac{180}{\pi} \sqrt{(S_\mathrm{h}^2 + 2S_\mathrm{h}) \frac{h^2}{r^2}}. \tag{5}$$

This analytical model shows that the rotation due to hygroscopic swelling θ_h is proportional to the height h and inversely proportional to the radius r of the shell, while being independent of its thickness t. To what extent these relations are true will be subject to further investigation.

C. Numerical simulation

To investigate the influence of the three main parameters on the performance of the HRA, numerical simulations are performed. The shell is modelled as a NURBS-surface using a custom IGA software package [25]. An orthotropic material

model is implemented on the surface. Only one half of the surface is simulated, since symmetry along the vertical axis is assumed.

Radius r and height h are discretized to 10 control points in u-direction (horizontal) and 100 in v-direction (vertical). To realize the constraints of the design, the control points along the bottom edge are fixed to restrict translation in all directions, realizing a clamping constraint. The control points on the top edge are constrained in z-direction only, allowing for movement in the xy-plane but maintaining the 90 degree angle between the central axis and top edge. To further simulate a clamping condition, the control points of both the top and bottom edges are rigidly connected to their vertical neighbours and these connections are forced to maintain a 90 degree angle with the xy-plane.

To enable symmetry, the nodes along the centreline are constraint in xyz-translation. Their rotations are kept free in order to allow the surface to twist. The top and bottom control points of the vertical centreline are defined as clamping points and can be used to measure or impose torques and rotations about the z-axis. See figure 4b for an overview of the constraints imposed on the model.

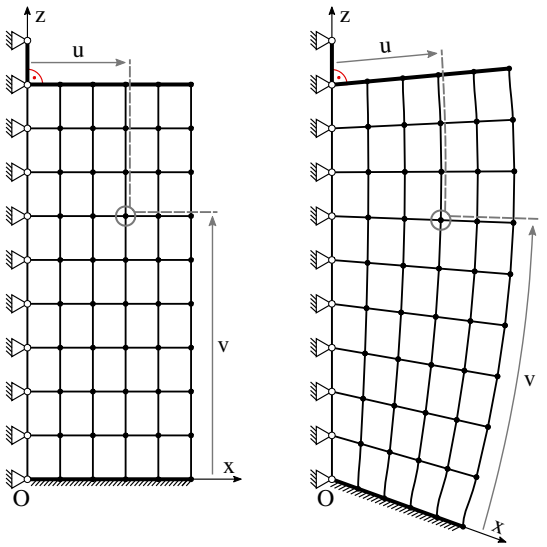

(a) Undeformed model, 2D view. The uv-coordinates for an arbitrary node are shown.

(b) Deformed model, 3D view. The uv-coordinates of the node move with the shell.

Figure 4: Schematic of the geometry as implemented in the numerical model. A surface is parameterized by defining nodes in u-direction and v-direction. By definition, these directions are tangent to each location of the surface. The implemented translational constraint along the vertical centreline and the clamping constraints along the horizontal top and bottom edges are also shown.

A central geometry is chosen, with dimensions 30 mm by 70 mm by 0.62 mm ($r \cdot h \cdot t$). From this geometry, radius, height and thickness are independently varied in positive and negative direction to generate a variety of geometries. For each of these geometries, the hygroscopic engineering strain S_h is imposed on the shell in the (initially vertical) v-direction. This deforms the geometry so that the resulting angle can be determined. An initial disturbance and a small initial twist are implemented to help the simulation overcome buckling, and to force the deformation to be anticlockwise to its undeformed state (see figure 2).

To compare the angles resulting from the numerical model with those resulting from the simulations for each parameter of interest, a Root Mean Square Error (RMSE) is used. It is defined as

$$\mathrm{RMSE} = \sqrt{\frac{1}{n}\sum_{i=1}^{n}(\theta_{\mathrm{ha},i} - \theta_{\mathrm{hs},i})^2}, \tag{6}$$

where n is the amount of solved geometries for each parameter of interest. Angles $\theta_{\mathrm{ha},i}$ and $\theta_{\mathrm{hs},i}$ are the analytical and numerical resulting angles of geometry i, respectively.

To investigate torque, seven deformed geometries are chosen (table 1): the central geometry, and for each design parameter a value near the beginning and end of the simulated range. A rotational displacement is gradually imposed on the upper clamping point of the surface, while measuring the torque exerted on the bottom clamping point about the z-axis.

Version	Radius r (mm)	Height h (mm)	Thickness t (mm)
A	30	70	0.62
B	30	40	0.62
C	30	100	0.62
D	10	70	0.62
E	50	70	0.62
f	30	70	0.32
g	30	70	1.22

Table 1: Dimensions of the geometries that were subjected to torque-simulations. Versions denoted in capitals (A-E) were also produced and tested as prototypes.

This rotation consists of two steps. Before starting to measure the torque on the bottom clamping point, an additional anticlockwise rotation θ_a of 30 degrees is imposed, stretching the geometry beyond its deformed state. Second, a clockwise rotation is imposed while measuring the torque. This final clockwise rotation consists of twice the resulting angle θ_h and twice the additional angle θ_a, stretching the geometry again. These steps are taken to determine the behaviour beyond the hygromorphic deformation. Figure 5 shows the complete sequence of rotation, including the initial resulting angle θ_h.

D. Prototype Realisation

In order to verify the simulations, five different geometries were built and tested. These geometries were chosen to correspond with the choices made for the simulated geometries. The central geometry A was built, as well as geometries towards the ends of the simulated spectrum of height (geometries B and C) and radius (geometries D and E), in both positive and negative direction. The thickness has not been varied in the physical tests, due to the lack of availability of veneer slices with the same properties but different thickness. See table 1 for an overview of the dimensions of the prototypes.

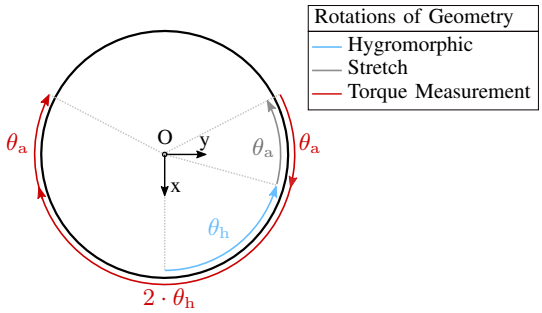

Figure 5: Schematic showing the different rotations subjected to the geometries, depicted from above. The hygromorphic rotation (θ_h) is caused by exposure to water. The stretching rotation (θ_a) and the torque measurement rotation ($2\theta_a + 2\theta_h$) are caused by applying a rotation on the top clamping point.

Because of its orthogonal properties, most notably the direction-dependant expansion [23], wood was chosen as hygro-responsive material. Performance of thin slices of wood (veneer) has proven to be sufficient for actuator applications [19]. When exposed to water, these veneer slices elongate perpendicular to their fibre direction only; they maintain their length parallel to the fibre.

The veneer slices were glued in 3D printed PLA clamps (Prusa Mk3s) with their fibres oriented horizontally. These clamps keep a perpendicular angle between the vertical centreline and the top and bottom edges of the shell. The necessary constraint along the vertical centreline was realized by taking two narrow rods of wood with the fibre in the vertical direction and glueing them to the middle of the veneer on either side. This bond of wood on wood proved to maintain its integrity in most cases, even after being exposed to water with the resulting large deformations. An example of a produced prototype is shown in figure 6.

E. Prototype Material Properties

Beech veneer was chosen as the hygro-active material for the HRA prototypes. In preliminary tests, it showed to have a sufficient elongation while maintaining its structural integrity during large deformations.

Some material properties needed to be determined for implementation in the orthotropic material model used in the numerical simulations. Hygroscopic expansion was measured by soaking five slices of veneer in water and measuring their dimensions before and after soaking. This resulted in an average elongation of 8.4% perpendicular to the fibre direction. No elongation parallel to the fibre direction occurred.

The Young's moduli were determined by performing a three-point bending test on five slices of veneer in both dry and wet state, resulting in a Young's modulus perpendicular to the fibre (E_T) of 174.16 MPa and a Young's modulus parallel to the fibre (E_L) of 4369.17 MPa.

These values are lower than those found in literature, although values in literature vary a lot [26]–[28]. This is probably due to the fact that in this case, the wood is completely soaked, whereas in literature a lower water content

(a) A specimen of prototype D in dry, undeformed state.

(b) A specimen of prototype D in wet, deformed state.

Figure 6: Dry and wet state of prototype D, with a radius of 10 mm and a height of 70 mm. The thin slice of darker wood serves as the centreline constraint and is glued on the veneer at both sides. The grey 3D printed parts serve both as constraint of top and bottom edge, and as connection interface between prototype and torsion machine.

is used [27]. Furthermore, the wood used could be a different species of beech with a different density. Young's moduli of wood are known to decrease with increasing water content and vary with different species and densities [23].

Lastly, the shear modulus G_{LT} and Poisson's ratio ν_{LT} are needed. The shear modulus was determined by calculating the ratio between mean values of E_L and G_{LT} from literature [26] and applying this ratio to the experimentally determined E_L of the veneer, resulting in a value of 781.25 MPa. Since the Poisson's ratio doesn't depend much on water content, it was determined from literature [26], resulting in a value of 0.048. An overview of the material properties is given in table 2.

	Young's Modulus		Shear Modulus	Poisson's	Strain
	E_L (MPa)	E_T (MPa)	G_{LT} (MPa)	ν_{LT} (-)	E_T (-)
Dry	5619.54	207.23	356.85	0.048	-
Wet	4369.17	174.16	277.44	0.048	0.084

Table 2: Overview of the dry and wet material properties used in the numerical simulations.

F. Test protocol

Each of the five prototype variations was fabricated five times, resulting in a total of 25 specimen. Each specimen was first soaked in water until no further rotation was noticed. It was then photographed from above. The resulting angle θ_h was determined using the image analysis software ImageJ [29].

Next, the specimen was placed in a torsion machine (Zwick Z005 with HBM T20WN torque meter). A rotational displacement was gradually imposed, while measuring the torque T on the bottom clamping point around the vertical axis. The same approach was taken as with the simulations, with additional rotations beyond the resulting angle θ_h of the

deformed geometry (see figure 5). In this case however, a smaller θ_a ranging from 5 to 20 degrees was applied, so that the prototypes would not break before test completion.

From the angle measurements, boxplots were created to be able to compare the experimental resulting angles to the angles derived from the analytical model and the numerical simulations. For each of the prototypes A to E, the torque-rotation graphs of the successful specimen were interpolated to obtain the average torque-rotation graph for that specimen. This could then be compared to the results of the torque simulations.

III. Results

A. Hygromorphic Rotation

Figure 7 shows the angle resulting from the simulations for increasing height (orange dots, figure a) and radius (blue dots, figure b) respectively. Additionally, the grey lines show the resulting angle according to the analytical model, calculated using equation 5.

The numerically simulated angles from geometries with varying height and radius follow the same path as the analytically calculated angles, albeit with a difference. The Root Mean Square Error (RMSE) between the analytically and numerically calculated angles when varying height is 5.4 degrees. When varying radius, the RMSE is 8.1 degrees.

The influence of the thickness t on the resulting angle is depicted in figure 8. The numerically calculated angle fluctuates around the constant analytical angle, with an RMSE of 4.7 degrees.

The development of the vertical engineering strain at each horizontal location of the geometries A to E is depicted in figure 9, normalised as a percentage of the radius. Although the initial vertical strain imposed on the shell is 0.084 along its entire radius, the resulting vertical strain calculated from the actual elongation is not uniform along the radius. As imposed by the constraints, it is zero at the shell centreline. It increases towards the shell edge and overshoots the imposed strain. The amount of overshoot increases when radius decreases, being 50 % in the case of geometry D.

The graphs predicted by the numerical simulations show discontinuities. Figure 10 a and b show the geometries highlighted in figure 7b, before and after a discontinuity with a drop in resulting angle. These geometries differ in radius by only 0.1 mm, while having a difference in resulting angle of 15.51 degrees.

Taking a closer look at the deformed geometries at these discontinuities of the numerical simulation graphs, different buckling modes and edge wrinkles can be seen. A simplified representation of the wrinkling of the edge per segment of the resulting angle graph is shown in the insets in figures 7 and 8.

This edge-wrinkling is present to varying extent at all solved geometries. As seen in figure 7b, the shell edge maintains a similar shape per segment when increasing radius. At small radii few wrinkles with a small amplitude are present, growing in size and numbers at segments with larger radii. Varying height (figure 7a) shows a different behaviour. Here, the end of a segment shows multiple larger wrinkles, which get smoothed out when jumping to a next segment with a higher resulting angle. When height increases further, wrinkles form again, until the next jump in resulting angle.

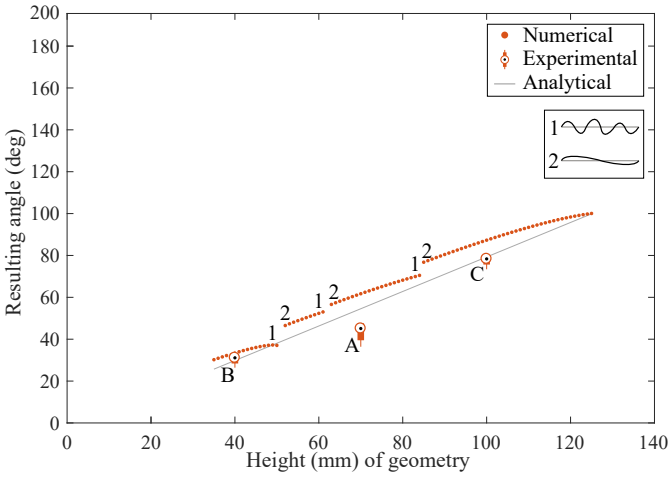

(a) Resulting angle of geometries with constant radius and varying height.

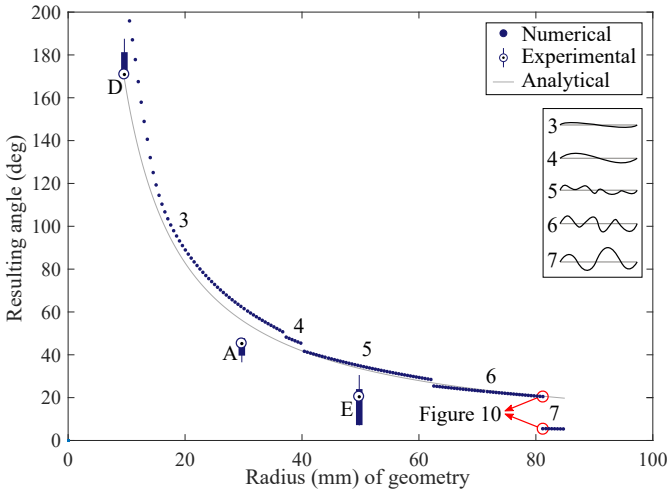

(b) Resulting angle of geometries with constant height and varying radius.

Figure 7: Resulting angle of geometries with constant radius and varying height (figure a), and a geometry with constant height and varying radius (figure b). Results of the simulation are depicted using dots. The grey lines show the angle from the theoretical calculation (equation 5). The results of the tested geometries are depicted with boxplots, with their labels corresponding to the prototype versions in table 1. The insets show a 2D-representation of the wrinkles of the edge at the numbered segments of the graphs.

The boxplots in figure 7 show the angular deformation of the tested prototypes. They show the same behaviour when radius or height varies, but their resulting angle is on average 20% lower than that of the numerical simulations. An example of a hygroscopically deforming prototype is displayed in movie S1, showing a time-lapse of a specimen of prototype D being exposed to water.

The prototypes also show similar buckling modes and wrinkling behaviour as the simulations. Within the same prototype there is a spread in resulting angle. This is most

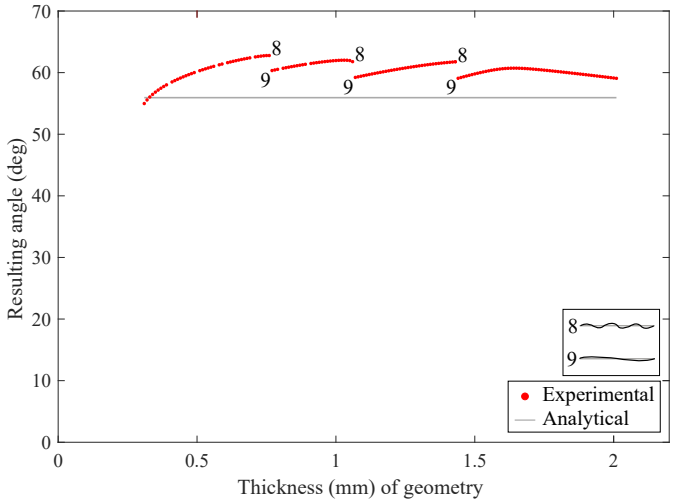

Figure 8: Resulting angle of geometries with constant radius and height, and varying thickness.

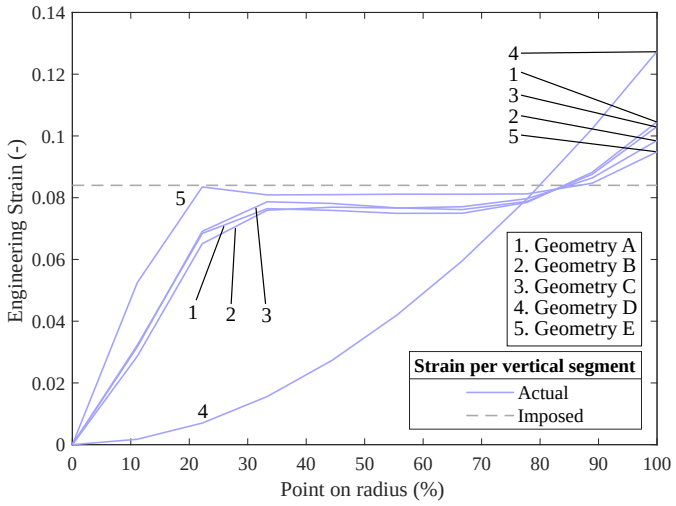

Figure 9: Engineering strain per vertical segment of the shell, for each of the five simulated geometries A-E. The grey dashed line represents the strain imposed on the shell in v-direction. At 100% of the radius, the strains of the geometries overshoot the imposed strain. Note that the radii of the five geometries are normalized.

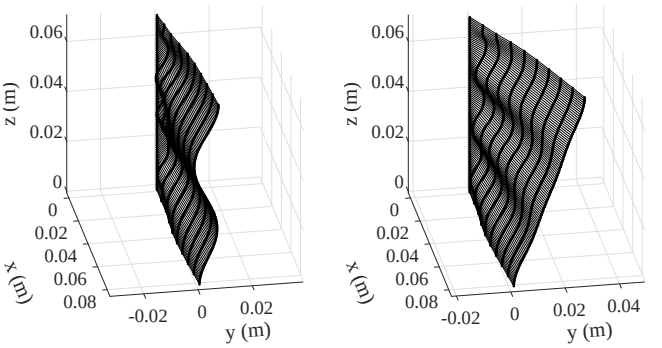

(a) Deformed geometry with a radius of 81.35 mm. Note the wrinkles of the shell edge, resulting in a rotation of 5.65 degrees.

(b) Deformed geometry with a radius of 81.25 mm. Note the smoother edge, resulting in a rotation of 21.16 degrees.

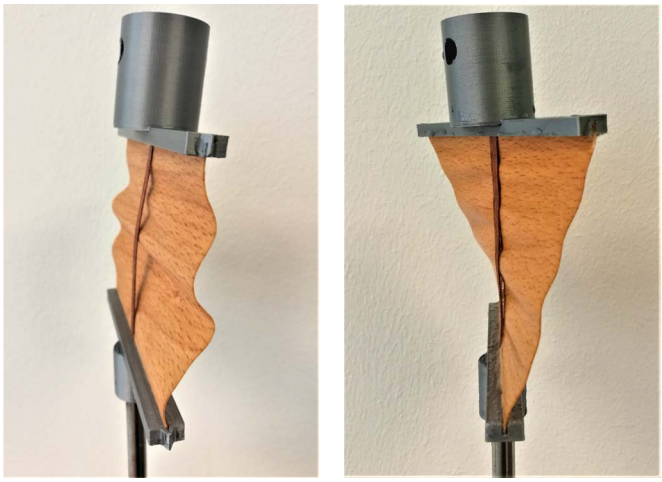

(c) A specimen of prototype E in wet state, with a rotation of 7.1 degrees. Debonding between the shell and the centreline constraint is present.

(d) A specimen of prototype E in wet state, with a rotation of 30.5 degrees.

Figure 10: Comparison of buckling modes of deformed geometries. Figure a and b show an example of a simulated geometry with a slightly different radius just before (a) and after (b) a discontinuity in resulting angle. The specific moment of this example is depicted in figure 7 with red circles. Figure c and d both show a wet specimen of prototype E, with a radius of 50 mm and a height of 70 mm.

notable when looking at various specimen of prototype E, depicted in figures 10 c and d. Its resulting angle ranges from 7.1 to 30.5 degrees.

B. Torque during rotation

The torque-rotation graphs of the five main geometries have been determined both numerically and experimentally. The left column of figure 11 shows the hygromorphically deformed geometry that is used as starting point for the torque simulations, together with the undeformed central geometry A (red outline). The middle column shows the numerical results (orange line) and the interpolated result of the tests (blue line) for each of the five geometries A to E. Additionally, the grey lines show the simulated torque during a rotation of a dry and undeformed shell.

The right column shows how each of the interpolated lines originates from the tested specimen. The grey lines show the different specimen that were tested per geometry. The torques of the tested geometries have been scaled by 0.5, since the prototypes consisted of two shells and the simulations only of one due to the symmetry across the centreline. Note that not all tests succeeded; some specimen failed during hygroscopic deformation, some failed halfway through the rotation sequence. Each tested prototype has at least three successfully tested specimen.

During rotation, the torques of the wet geometry are close to zero. As soon as the resulting angle is reached however, torque increases. The dry rotation shows this increase immediately when being rotated, without a region of zero torque.

No real trend is observed when looking at the torque

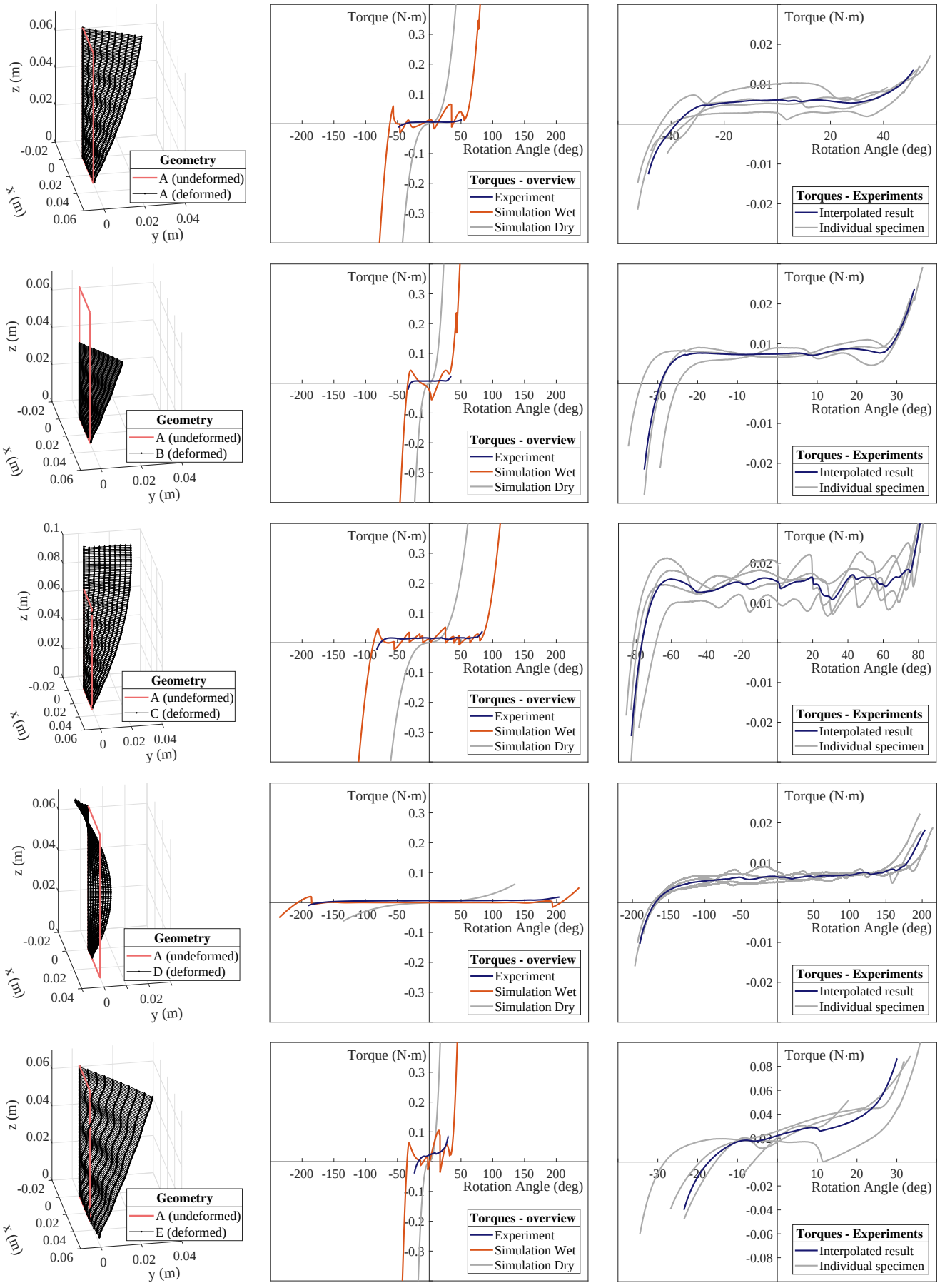

Figure 11: Deformed geometries and torque-graphs of the five simulated and tested geometries. (Caption continues on next page.)

Figure 11: (Continued from previous page.) The left column displays the hygroscopicly deformed geometries before being rotated back, together with the outline of the undeformed central geometry A in red. The middle column displays the torques of simulated geometries (orange lines) and the interpolated result of the tested prototypes (blue lines). Additionally, the simulated torque of a dry and undeformed geometries is shown in grey. The right column shows how the interpolated line for each prototype is determined from the tested specimen. Note that the scale of the y-axis is different from the one in the middle column.

graphs of different radii or heights, other than the transition region from positive to negative torque being larger with a larger resulting angle. The magnitude of the transition region of geometry E is highest, followed by geometry C.

The prototypes show similar behaviour. They too have a region of low torque. The torque in their region has smaller fluctuations but generally has a positive offset, whereas the torque in the transition region of the simulated geometries fluctuates around zero. The magnitude of the transition region fluctuates around 0.007 N·m for prototypes A, B and D, around 0.015 N·m for prototype C, and around 0.02 N·m for prototype E.

As shown in figure 12, the rotation-torque graphs of geometries with a varying thickness following from the simulations show similar behaviour as those of the rotation-torque graphs of geometries with varying radius and height. Within the hygromorphically deformed angular range, torque fluctuates around zero. Rotating the geometry beyond this range increases the torque. The height of the fluctuations does vary however. The peak-to-peak distance increases as the shell becomes thicker.

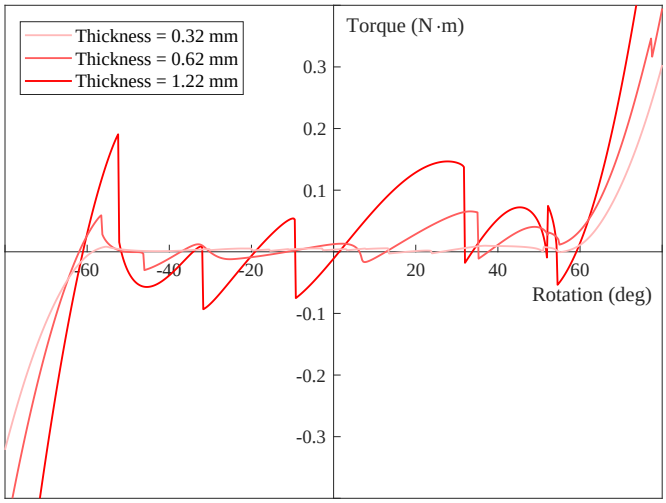

Figure 12: Torque during simulated back-rotation of three instances of geometry A, each with a different thickness.

IV. Discussion

A. Influence of Geometric Parameters on Resulting Angle

Looking at figures 7 a and b, height and radius prove to be valid parameters to design for a certain rotation of an HRA. Depending on the specific application and corresponding size, one of the two can be chosen, after which the other follows from the desired angular output.

The numerical simulations confirm the relation between h, r and θ_{h} from the analytical model of equation 5. The resulting angle θ_{h} increases proportionally as height h increases, and decreases as radius r increases. Unlike suggested by the analytical model, figure 8 shows that the resulting angle is not entirely independent of the thickness of the shell. Due to the increasing and decreasing number of wrinkles of the shell, the resulting angle slightly fluctuates around the analytical value when thickness is increased. This fluctuation is minimal however.

The difference between the resulting angles found in the analytical model and the numerical simulations can be explained by looking at the development of the strains in figure 9. The actual vertical engineering strain overshoots the imposed engineering strain at the shell edge. This means that the length of the outer edge of the shell L_{e} will be longer than calculated in equation 2, resulting in a larger angle.

Another difference between the analytical model and the numerical simulations, are the discontinuities in the graphs of the simulated angles. Taking the deformed geometries in figure 10 as an example, shown in figure 7 with red circles, a reason for these discontinuities can be seen. Although their radii differs only by 0.1 mm, the geometry in figure 10a buckles extensively, resulting in wrinkles along its edge. The part of the elongation that is used to create those wrinkles is not converted in a rotation. The edge of the geometry in figure 10b, however, is almost smooth and therefore a larger resulting angle is achieved.

Each line segment of the numerical calculations in figures 7 and 8 is thought to correspond to a certain buckling mode of the shell. Multiple parallel lines may exist, from which only segments are found when the numerical simulation jumps from one to the other. Multiple modes can exist in the same geometry, meaning that the same geometry can have different stable deformed instances, each of them with a different resulting angle. This behaviour resembles that of other multi-stable compliant shell mechanisms [30]–[33] and is shown in movie S2. What exactly causes this multi-stable behaviour and how it can be tweaked to fully exploit its benefits, remains subject for future research.

The observed buckling modes and multi-stability are also present within multiple specimen of the same prototype. Some specimen display a small angle with large wrinkles on the edge, but can be manually rotated to their maximum angle with smooth edge and maintain this position. Figures 10 c and d show an example of this phenomenon. The specimen of prototype E in figure 10c displays more and larger wrinkles, converting less elongation in a rotation than the specimen of prototype E in figure 10d.

B. Influence of Geometric Parameters on Torque

Once deformed, the HRA behaves like a zero-moment element, essentially straightening and elongating the crossover region from positive to negative torque. In its wet and deformed state, the geometry can be rotated back with a torque

close to zero, until the negative hygromorphic angle is reached.

Radius and height do not seem to have an influence on the magnitude of the torque, besides the fact that the zero-moment region is larger with a smaller radius or larger height. The thickness of the shell does have an influence on the peak-to-peak value of the oscillations in the zero-moment region of the rotation and on the slope of the rotation-torque graph outside of the zero-moment region. Both increase as thickness increases, suggesting that thickness can be used to tweak the torque-output during rotation. Further research is needed to quantify the influence of thickness on the torque.

The fluctuations of the torque in the zero-moment region of both the simulated and tested geometry are caused by wrinkles being formed or being stretched flat. This is displayed in more detail in movie S3, showing the back-rotation of a specimen of geometry C together with its torque-graph. Initially, a wrinkle will resist rotation, causing an increase in torque. Beyond a certain threshold, the shell rapidly jumps to another mode, releasing the build up stress. This manifests itself in the torque graphs as fluctuations around a value close to zero.

The positive offset of the torque graphs of the prototypes is supposedly due to the visco-elastic behaviour of the wood. The angle-torque graphs depend on the direction of the rotation. The graphs in the right column of figure 11 only show one direction; if the geometry would have been rotated back to the start position of the torque-test, a loop would form. More research is needed to further investigate the visco-elastic aspect of wood as a material for the HRA.

C. Comparing Numerical Simulation and Prototype Experiments

The observed differences between numerical simulations and experiments are small. The biggest difference lies within the zero-moment region of the torque graphs, which has bigger fluctuations in the simulations. The geometry is modelled as a perfect uniform shell, whereas the veneer used in the prototypes has imperfections. A perfect shell buckles more abruptly than an imperfect shell. This could explain the differences observed in the torque-graphs. Further investigation may improve simulation accuracy.

The lower resulting angles of the tested geometries can be explained by looking at the differences between the simulated model and the constructed prototypes. The most notable difference is the implementation of the constraint. The added thin slices of wood at each side of the shell stop the middle from elongating, but they also add extra rotational stiffness. They will resist angular deformation and therefore decrease the resulting angle of the deformed geometry. Likewise, the bonding between the slices of wood and the shell sometimes fails as a result of large buckling, as can be seen in figure 10c. This also causes a lower resulting angle.

The choice of veneer as a material for the HRA has proven to be advantageous. It is easily available and low-tech. However, some challenges arise from its unpredictability. Wood is known to have imperfections, which in this case causes a spread in behaviour between specimen and sometimes specimen fail before test completion.

Additionally, the form-freedom of veneer is limited to planar shells. For some applications it would be interesting to develop a more controllable material that can be shaped to a spatially curved shell, while maintaining its hygroscopic directional properties.

D. Real-life applications

The geometries treated in this paper can be of use in a number of applications. According to the analytical model, equal scaling of height h and radius r yields the same resulting angle θ_{h}. Scaling will be limited by material availability however, as the circular cross-section of trees limits the size of veneer with parallel fibres that can be produced. To design an HRA for larger applications, a different hygro-active material might be needed.

Similar to already existing systems [19], multiple HRA's could be placed on a building façade, regulating the airflow through the building in response to the environmental humidity. Due to the cylindrical movement space, they can be placed inside a pipe and will therefore stick out less than existing meteoro-sensitive façades.

Developing the placement inside pipes even further, the HRA could also be used to regulate waterflow in for instance irrigation systems. It can be designed to open a container of water during a period of drought, closing the container again when a certain volume of water has passed. A precise control of the rotation based on the influx of water in the material will be needed.

Alternatively, a different look on the HRA might provide another application. In constant-moment systems, pretension is needed to perform the constant-moment behaviour. By fixing both ends of the shell, the HRA provides a way of adding or subtracting pretension, thereby activating the system to enable its functionality.

Finally, the concept of a rotational motion due to selective restriction of an expansion does not limit itself to hygroscopic swelling only. Passive actuators could be designed to take advantage of other environmental gradients such as temperature, making the concept accessible for more high-tech applications and materials.

V. Conclusion

A Hygromorphic Rotational Actuator has been designed by selectively restricting the direction-dependent hygroscopic elongation of a compliant shell. The HRA is capable of deforming its own geometry, and therefore matches the observed behaviour in the plant world and that of other hygromorphic actuators. The simplicity of the HRA is its greatest asset; it operates without the need of additional sensors, motors and control units, and it does so with a minimum amount of parts.

The presented design adds to the possibilities of passive hygromorphic actuators and can be used as a building block in larger compliant systems. Its range of motion can be tweaked by selecting the radius and height of the shell. The shell's thickness does not have a notable influence on its kinematic

behaviour. It does seem to influence the magnitude of the torque, this should be investigated in more detail.

The multi-stable and zero-moment behaviour are interesting aspects of the HRA that can further expand its usage. Being able to precisely control these aspects remains subject for future research,

ACKNOWLEDGEMENTS

The authors would like to thank the lab technicians of the Department of Precision and Microsystem Engineering of the TU Delft for providing help and advice in the design of the experimental setup.

SUPPLEMENTARY MATERIAL

Movie S1 Timelapse of HRA Movement
Movie S2 Multi-stable Behaviour of the HRA
Movie S3 Real-time Torque Test of the HRA

REFERENCES

[1] A. Sakes, M. D. Van Wiel, P. W. Henselmans, J. L. Van Leeuwen, D. Dodou, and P. Breedveld, "Shooting mechanisms in nature: A systematic review," *PLoS ONE*, vol. 11, no. 7, pp. 1–46, 2016.

[2] R. Elbaum, L. Zaltzman, I. Burgert, and P. Fratzl, "The role of wheat awns in the seed dispersal unit," *Science*, vol. 316, no. 5826, pp. 884–886, 2007.

[3] S. Joosten, G. Radaelli, and H. Vallery, "Compliant Shell Deformation in Plants : A Designer's Toolbox," Delft University of Technology, Tech. Rep., 2019. [Online]. Available: http://resolver.tudelft.nl/uuid:d04ae322-73ad-4f27-bfb5-5cead96a8e65

[4] J. Dumais and Y. Forterre, "Vegetable Dynamicks: The Role of Water in Plant Movements," *Annual Review of Fluid Mechanics*, vol. 44, no. 1, pp. 453–478, 2011.

[5] V. Charpentier, P. Hannequart, S. Adriaenssens, O. Baverel, E. Viglino, and S. Eisenman, "Kinematic amplification strategies in plants and engineering," *Smart Materials and Structures*, vol. 26, no. 6, pp. 63 002 – 63 002, 2017.

[6] R. Elbaum, "Structural Principles in the Design of Hygroscopically Moving Plant Cells," in *Plant Biomechanics: From Structure to Function at Multiple Scales*, A. Geitmann and J. Gril, Eds. Sainte-Anne-de-Bellevue, QC: Springer International Publishing, 2018, pp. 235–245.

[7] E. Reyssat and L. Mahadevan, "Hygromorphs: From pine cones to biomimetic bilayers," *Journal of the Royal Society Interface*, vol. 6, no. 39, pp. 951–957, 2009.

[8] M. Hayashi, S. P. Gerry, and D. J. Ellerby, "The seed dispersal catapult of Cardamine parviflora (Brassicaceae) is efficient but unreliable," *American Journal of Botany*, vol. 97, no. 10, pp. 1595–1601, 2010.

[9] H. Liang and L. Mahadevan, "Growth, geometry, and mechanics of a blooming lily," *Proceedings of the National Academy of Sciences*, vol. 108, no. 14, pp. 5516–5521, 2011. [Online]. Available: http://www.pnas.org/cgi/doi/10.1073/pnas.1007808108

[10] H. Kobayashi, B. Kresling, and J. F. Vincent, "The geometry of unfolding tree leaves," *Proceedings of the Royal Society B: Biological Sciences*, vol. 265, no. 1391, pp. 147–154, 1998.

[11] T. Speck, G. Bold, T. Masselter, S. Poppinga, S. Schmier, M. Thielen, and O. Speck, "Biomechanics and Functional Morphology of Plants - Inspiration for Biomimetic Materials and Structures," in *Plant Biomechanics: From Structure to Function at Multiple Scales*, 1st ed., A. Geitmann and J. Gril, Eds. Cham: Springer International Publishing, 2018, ch. 4, pp. 399 – 433.

[12] S. Schleicher, J. Lienhard, S. Poppinga, T. Speck, and J. Knippers, "A methodology for transferring principles of plant movements to elastic systems in architecture," *CAD Computer Aided Design*, vol. 60, pp. 105–117, 2015. [Online]. Available: http://dx.doi.org/10.1016/j.cad.2014.01.005

[13] S. Poppinga, C. Zollfrank, O. Prucker, J. Rühe, A. Menges, T. Cheng, and T. Speck, "Toward a New Generation of Smart Biomimetic Actuators for Architecture," *Advanced Materials*, vol. 30, no. 19, pp. 1–10, 2018.

[14] I. Burgert and P. Fratzl, "Actuation systems in Plants as prototypes for bioinspired devices," *Philosophical Transactions of the Royal Society A: Mathematical, Physical and Engineering Sciences*, vol. 367, no. 1893, pp. 1541–1557, 2009.

[15] M. Rüggeberg and I. Burgert, "Bio-Inspired wooden actuators for large scale applications," *PLoS ONE*, vol. 10, no. 4, pp. 1–16, 2015.

[16] L. Zhang, S. Chizhik, Y. Wen, and P. Naumov, "Directed Motility of Hygroresponsive Biomimetic Actuators," *Advanced Functional Materials*, vol. 26, no. 7, pp. 1040–1053, 2016.

[17] K. M. Al-Obaidi, M. Azzam Ismail, H. Hussein, and A. M. Abdul Rahman, "Biomimetic building skins: An adaptive approach," *Renewable and Sustainable Energy Reviews*, vol. 79, no. May, pp. 1472–1491, 2017.

[18] D. M. Wood, D. Correa, O. D. Krieg, and A. Menges, "Material computation-4D timber construction: Towards building-scale hygroscopic actuated, self-constructing timber surfaces," *International Journal of Architectural Computing*, vol. 14, no. 1, pp. 49–62, 2016.

[19] S. Reichert, A. Menges, and D. Correa, "Meteorosensitive architecture: Biomimetic building skins based on materially embedded and hygroscopically enabled responsiveness," *CAD Computer Aided Design*, vol. 60, pp. 50–69, 2015. [Online]. Available: http://dx.doi.org/10.1016/j.cad.2014.02.010

[20] B. Shin, J. Ha, M. Lee, K. Park, G. H. Park, T. H. Choi, K. J. Cho, and H. Y. Kim, "Hygrobot: A self-locomotive ratcheted actuator powered by environmental humidity," *Science Robotics*, vol. 3, no. 14, pp. 1–9, 2018.

[21] D. Raviv, W. Zhao, C. McKnelly, A. Papadopoulou, A. Kadambi, B. Shi, S. Hirsch, D. Dikovsky, M. Zyracki, C. Olguin, R. Raskar, and S. Tibbits, "Active printed materials for complex self-evolving deformations," *Scientific Reports*, vol. 4, no. 7422, pp. 1–8, 2014.

[22] R. M. Erb, J. S. Sander, R. Grisch, and A. R. Studart, "Self-shaping composites with programmable bioinspired microstructures," *Nature Communications*, vol. 4, pp. 1–8, 2013.

[23] David E. Kretschmann, "Mechanical Properties of Wood," in *Wood Handbook - Wood as an Engineering Material*, centennial ed., R. J. Ross, Ed. Madison, WI: U.S. Dept. of Agriculture, Forest Service, Forest Products Laboratory, 2010, ch. 5, pp. 5–1 – 5–45. [Online]. Available: www.fpl.fs.fed.us

[24] H. Steinhaus, "Squirels, Screws, Candles, Tunes, and Shadows," in *Mathematical Snapshots*, 3rd ed. Mineola, New York: Dover Publications, Inc., 1983, pp. 229–230.

[25] A. P. Nagy, "Isogeometric Design Optimisation," Ph.D. dissertation, Delft University of Technology, 2011. [Online]. Available: http://resolver.tudelft.nl/uuid:de6aef44-7d24-49aa-9485-064c52a147fa

[26] S. Hering, D. Keunecke, and P. Niemz, "Moisture-dependent orthotropic elasticity of beech wood," *Wood Science and Technology*, vol. 46, no. 5, pp. 927–938, 2012.

[27] P. Niemz, T. Ozyhar, S. Hering, and W. Sonderegger, "Moisture Dependent Physical-Mechanical Properties from Beech Wood in the Main Directions," *Pro Ligno*, vol. 11, no. 4, pp. 37–42, 2015.

[28] E. Güntekin, T. Y. Aydin, and P. Niemz, "Some orthotropic elastic properties of fagus orientalis as influenced by moisture content," *Wood Research*, vol. 61, no. 1, pp. 95–104, 2016.

[29] C. A. Schneider, W. S. Rasband, and K. W. Eliceiri, "NIH Image to ImageJ: 25 years of image analysis," *Nature Methods*, vol. 9, no. 7, pp. 671–675, 2012.

[30] K. A. Seffen, "Hierarchical multi-stable shapes in mechanical memory metal," *Scripta Materialia*, vol. 56, no. 5, pp. 417–420, 2007.

[31] J. P. Udani and A. F. Arrieta, "Analytical Modeling of Multi-sectioned Bi-stable Composites: Stiffness Variability and Embeddability," *Composite Structures*, vol. 216, no. February, pp. 228–239, 2019. [Online]. Available: https://doi.org/10.1016/j.compstruct.2019.02.015

[32] H. Yang and L. Ma, "1D to 3D multi-stable architected materials with zero Poisson's ratio and controllable thermal expansion," *Materials and Design*, vol. 188, pp. 1–16, 2020.

[33] A. F. Arrieta, V. Van Gemmeren, A. J. Anderson, and P. M. Weaver, "Dynamics and control of twisting bi-stable structures," *Smart Materials and Structures*, vol. 27, no. 2, 2018.

3

Additional Geometric Properties

3.1. Scaling a Geometry

To investigate the effect of scaling, geometry A is numerically simulated using different scaling factors (see appendix D.2). Two types of scaling are performed, one only scaling radius and height, and one scaling radius, height and thickness.

Figure 3.1a shows the influence of scaling on the resulting angle for both situations. According to the analytical model (equation 2.5) the angle should not change when scaling a geometry. A slight decrease in angle is however present with increasing scaling factor.

The vertical strain of the shell might give an explanation for this decrease. As shown in figure 3.1b, the final strain of the outer edge (100% of radius) decreases as scaling factor F_s increases. This is probably due to the fact that, in a larger geometry, there is more horizontal space to redistribute the vertical strain close to the shell centreline.

The strain graphs in figure 3.1b belong to geometries that have their radius and height scaled only. When including thickness in the scaling as well, the difference in strain at 100% of the radius is less pronounced. Scaling r, h and t does result in a larger drop in rotation however. This is due to the fact that wrinkling of the edge increases when increasing thickness, see the insets in figure 3.1a. These phenomena are similar to observations in figures 7 and 8 of chapter 2. The wrinkles reduce the amount of elongation that is being converted into a rotation.

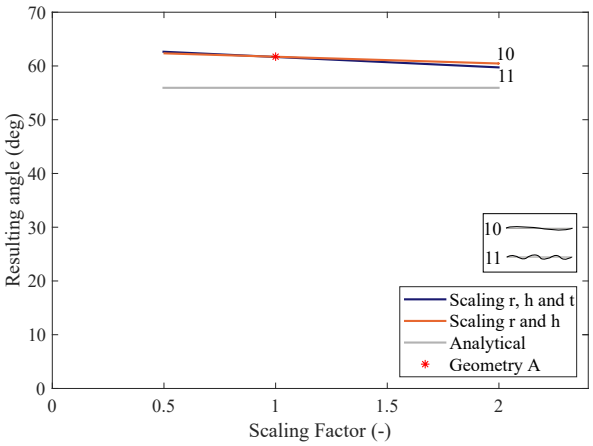

(a) Effect of scaling Geometry A (red star) on the resulting angle. Two types of scaling are performed, one only scaling radius and height (blue line), and one also scaling thickness (orange line). The constant analitical model is depicted with a grey line. The insets show the shape of the wrinkles of the edge for each of the two scaling methods.

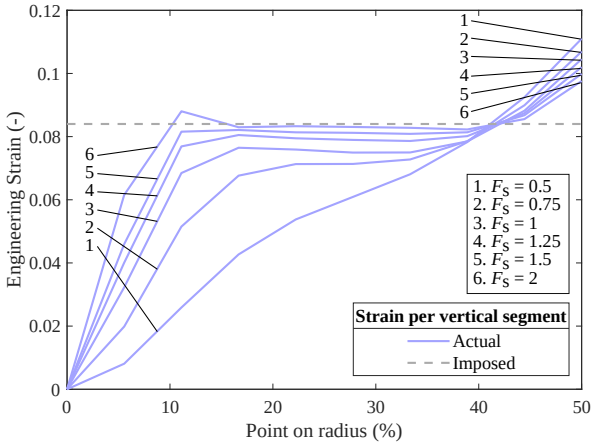

(b) Engineering strain from shell centreline (0%) to shell outer edge (100%) for geometries scaled with different scaling factors F_s.

Figure 3.1: Different aspects of the behaviour of scaled geometries.

3.2. Influence of Initial Twist

3.2.1. Concept

A parameter of interest other than radius, height and thickness, is initial twist τ (figure 3.2). An immediate advantage of adding initial twist to a geometry, is fixing the preferred direction of rotation. While the direction of hygromorphic rotation of regular HRA's is determined by things like material irregularities, initial twist forces this rotation to be in its same direction. To investigate other properties of geometries with initial twist, an updated analytical model is build and additional numerical simulations are performed.

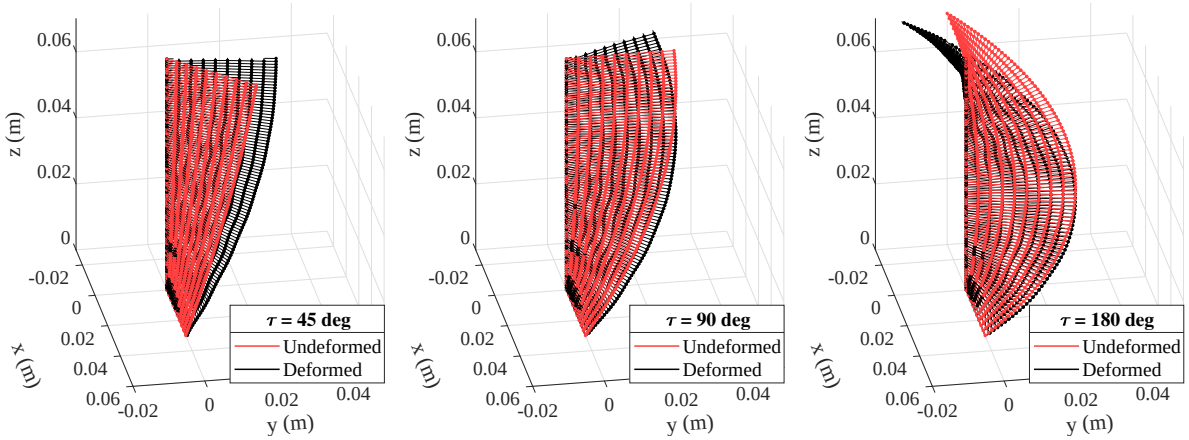

(a) Geometry h: initial twist of 45 degrees ($\tau = \frac{1}{8}$).

(b) Geometry i: initial twist of 90 degrees ($\tau = \frac{1}{4}$).

(c) Geometry j: initial twist of 180 degrees ($\tau = \frac{1}{2}$).

Figure 3.2: Various versions of Geometry A with an initial twist. The deformed geometry is shown in black, the undeformed geometry is shown in red.

3.2.2. Updated Analytical Model

Instead of an initially straight edge with length equal to the length of the centreline, this time the outer edge already has a certain amount of spiralling. Adapting equation 2.1 to obtain the length of the undeformed edge $L_{e,u}$ with initial twist τ:

$$L_{e,u} = \tau \cdot \sqrt{H^2 + C^2} = \tau \cdot \sqrt{\left(\frac{h}{\tau}\right)^2 + (2\pi)^2 \cdot r^2}, \tag{3.1}$$

where τ is the twist expressed as amount of completed turns of the upper edge, H is the height of the helix with one completed turn, C is the circumference of the cylinder, r is the radius of the cylinder enveloping the helix, and h is the height of the actual geometry at which the amount of turns τ are completed.
The rotation in degrees θ_u between the upper edge of this geometry in undeformed state with respect to the upper edge of a shell with no initial twist, is just a fraction of a full rotation of 360 degrees:

$$\theta_u = 360 \cdot \tau. \tag{3.2}$$

The new length of the edge of the shell after hygromorphic deformation $L_{e,d}$ is calculated analogous to equation 2.2. In stead of height h, $L_{e,u}$ is taken as initial length:

$$L_{e,d} = L_{e,u} \cdot (1 + S_h), \tag{3.3}$$

where S_h is the engineering strain due to hygroscopic swelling.
The deformed length can then be used analogous to equations 2.3 to 2.5 to obtain the rotation of the deformed geometry with respect to a shell with no initial twist. For an arbitrary rotation of $i\pi$ radians:

$$L_{e,u} \cdot (1 + S_h) = \sqrt{h^2 + C^2} = \sqrt{h^2 + (i\pi)^2 \cdot r^2}, \tag{3.4}$$

$$i\pi = \sqrt{\frac{\left(L_{e,u} \cdot (1 + S_h)\right)^2 - h^2}{r^2}}. \tag{3.5}$$

Rearranging terms and generalizing to obtain the rotation of the deformed shell θ_d in degrees yields

$$\theta_d = \frac{180}{\pi}\sqrt{\frac{\left(L_{e,u}\cdot(1+S_h)\right)^2 - h^2}{r^2}}. \tag{3.6}$$

Substituting $L_{e,u}$ with equation 3.4 gives

$$\theta_d = \frac{180}{\pi}\sqrt{\frac{\left(h^2+4\pi^2r^2\tau^2\right)\cdot\left(S_h^2+S_h+1\right)-h^2}{r^2}}, \tag{3.7}$$

$$\theta_d = \frac{180}{\pi}\sqrt{\left(S_h^2+2S_h\right)\frac{h^2}{r^2}+\left(S_h^2+S_h+1\right)\frac{2\pi^2\tau^2}{r^2}}. \tag{3.8}$$

To obtain the final hygromorphic rotation of an HRA with initial twist, the undeformed angle needs to be subtracted from this result:

$$\theta_h = \theta_d - \theta_u = \theta_d - 360\tau. \tag{3.9}$$

3.2.3. Numerical Simulation of Initial Twist

Using Geometry A as a starting point, initial twist is increased step by step (see section D.2), while calculating the resulting angle. Figures 3.2 a to c show the undeformed and deformed geometries for initial twist of 45, 90 and 180 degrees, respectively. Figure 3.3a shows the angle resulting from the numerical simulations (blue dots) as well as the angle resulting from the analytical model of equations 3.8 and 3.9.
When initial twist increases, the resulting angle of the numerical simulation first decreases, after which it becomes almost constant at around 120 degrees of initial twist. After that, it slightly increases again. The analytical model shows a different behaviour after 120 degrees of initial twist. The resulting angle increases much quicker than the results of the numerical simulations.
This behaviour can be explained by looking at the graphs in figure 3.3b. Here the angle of the initial twist θ_u (equation 3.2), the resulting angle compared to a straight undeformed shell θ_d and the actual resulting angle of an initially twisted geometry θ_h are plotted. While θ_u depends on τ linearly, θ_d and τ have a more complex relation. During small initial twist, the subtraction of θ_u from θ_d has a large influence on the resulting angle θ_h. As the size of τ increases, however, θ_d increases quadratically. Its influence on equation 3.9 becomes bigger, increasing the resulting angle θ_h.

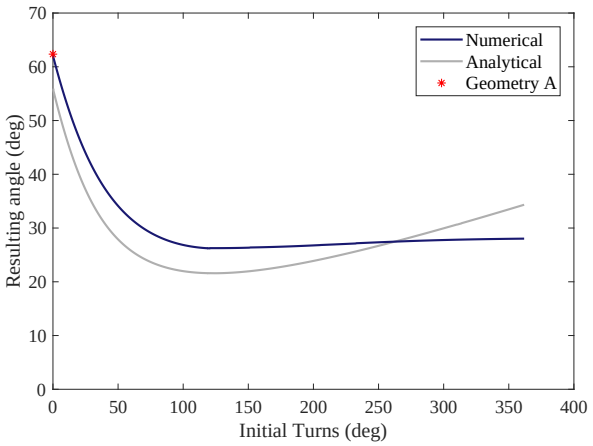

(a) Resulting angle of geometries with constant radius, height and thickness, but with varying initial rotation. The blue line depicts the result of the numerical simulations, the grey line shows the analytical model according to equation 3.9.

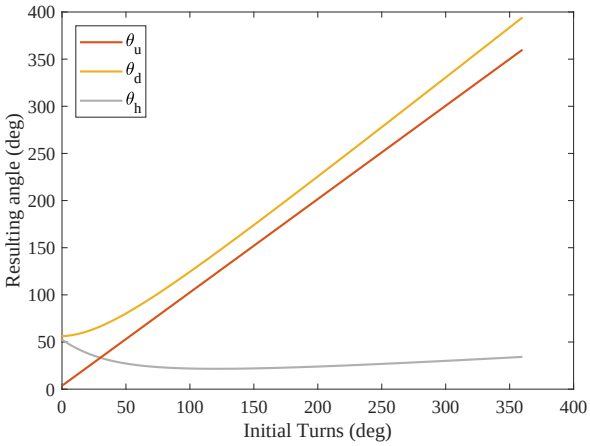

(b) Graph showing how, in the analytical model, θ_h is constructed from θ_u and θ_d (equations 3.2 to 3.9).

Figure 3.3: Different aspects of the behaviour of geometries with an initial rotation.

4

Additional Considerations

4.1. Visco-Elastic Behaviour

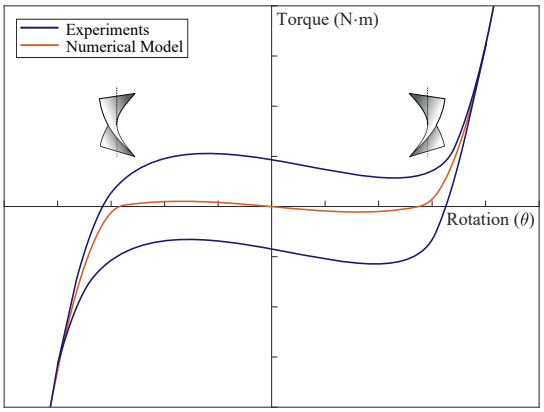

Figure 4.1: Schematic representation of the difference between the rotation-torque graphs of the numerical model (blue line) and the tested prototypes (red line).

A possible explanation for the positive offset of the measured torque in the zero moment region of figure 2.11, is given in section IV of chapter 2. Some further thoughts are provided here.

It is thought that the prototypes show visco-elastic behaviour, meaning that the torque follows a different path when the geometry is rotated clockwise then when it is rotated anticlockwise. This loop is schematically shown in red in figure 4.1. In the experiments, the prototypes are only rotated in one direction and thus only the upper half of the loop is found.

To verify this suspicion, further research is needed. Experiments need to be conducted that rotate the prototypes back to their initial deformed state. To achieve this, careful consideration needs to be put in the determination of θ_a in order to keep the specimen intact during the additional rotation.

4.2. Energy of the Shell

The behaviour of the wet and deformed geometry as a zero-moment element is further investigated by looking at the energy of the shell at various points during the rotation. Figure 4.2 shows again the angle-torque graph of Geometry A, resulting from the torque simulation. The labels E1 to E6 depict certain points of interest, right before or after discontinuities in the graph.

The energy of the shell at these points of interest is shown in figures 4.3 a to e. It is determined by taking the integral in u-direction of the shell, for each horizontal segment along the edge in v-direction. In each of these cases, the energy oscillates around about 0.007 J/m. The surface area below each of these lines represents the total energy E_{tot} contained in the shell.

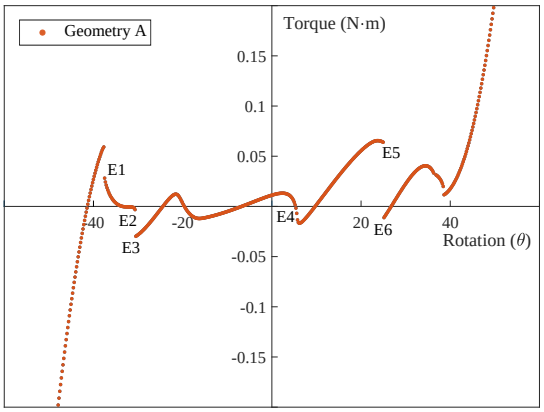

Figure 4.2: Torque-rotation graph of Geometry A, generated with numerical simulations. The labels E1-E6 depict points of interest, of which the energy of the edge is presented in figures 4.3 a to f.

Although each graph has a different shape due to the different state of the wrinkles of the shell edge, the total energy does not vary much between the different graphs of figure 4.3. This further confirms the theory of the wet HRA being a zero-moment element.

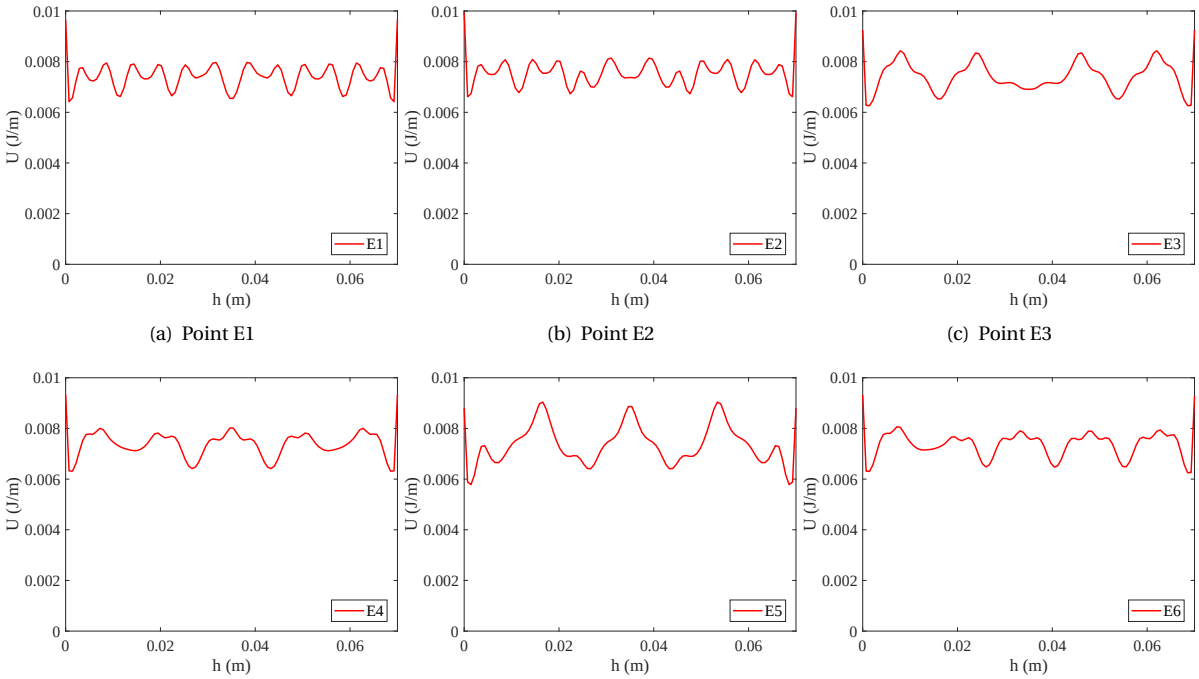

(a) Point E1 (b) Point E2 (c) Point E3

(d) Point E4 (e) Point E5 (f) Point E6

Figure 4.3: Energy contained in the shell at each horizontal segment along the height of the shell, for each of the six points of interest in figure 4.2.

The energy contained in the shell is an interesting measure of the performance of the HRA, and could be used more extensively in its future analysis. Optimisation for a certain energy level or a certain shape of the energy graph at given points can guide the choice of the important parameters.

Appendix

A

Fabrication of the HRA

A.1. Goal of Prototypes

During the design process, a lot of different fabrication methods were tried and investigated. Some methods were only used to rapidly test ideas, others were tried to see if they suited production of actual prototypes. This chapter will discuss these production methods, their performance and their limitations. Next, an overview of the final prototype fabrication is presented. Finally, some promising fabrication methods from literature that could improve the performance of the HRA are presented.
The starting point in all the fabrication methods, is the implementation of the elongation constraints as mentioned in section 2.II-A.

- Hygroscopic expansion in vertical direction
- Constraint 1: Restriction of expansion along the vertical centreline of the shell
- Constraint 2: Maintaining a 90 degree angle between the centreline and the top and bottom edges of the shell

Occasionally a constraint was simplified or left out to investigate the feasibility of some methods.

A.2. Early Prototypes

As stated in chapter 2.II-D, veneer is a low-cost, easy to use material to build hygromorphic actuators with [19]. Before arriving at the final prototype, different variations of the design have been build using veneer as the hygro-active material. All of these use the direction-dependent swelling of the veneer to generate the rotation, but they use different methods of implementing the constraints. In al cases, beech veneer was used as material for the shell.

A.2.1. Veneer and Cloth

As a first test of the concept of a selectively restricted hygro-active shell, a piece of cloth was glued to a slice of wood (veneer) on both sides (figure A.1a). After exposure to water, the shell showed a rotation of its upper edge with respect to its bottom edge (figure A.1b). This result was promising, however it showed additional unwanted deformation of the centreline (figure A.1c). It also proved difficult to align the cloth and the shell properly.
To try to counteract the curvature of the centreline, two slices of veneer were added to the geometry to form a plus-shape. This plus-shape was glued in place in a 3D-printed base, partially fulfilling constraint 2. The added stability aids in maintaining the vertical orientation of the centreline. The resulting geometry can be seen in dry and wet state in figure A.2.
The added shells kept the geometry upright. The wet geometry showed a small rotation. After exposure to water, the structure lost its plus-shape however. The shells shifted away from the centreline (figure A.2b and d). Buckling of the shell's edges wass also present. These phenomena, in combination with the absence of the top constraint, reduced the resulting rotation.

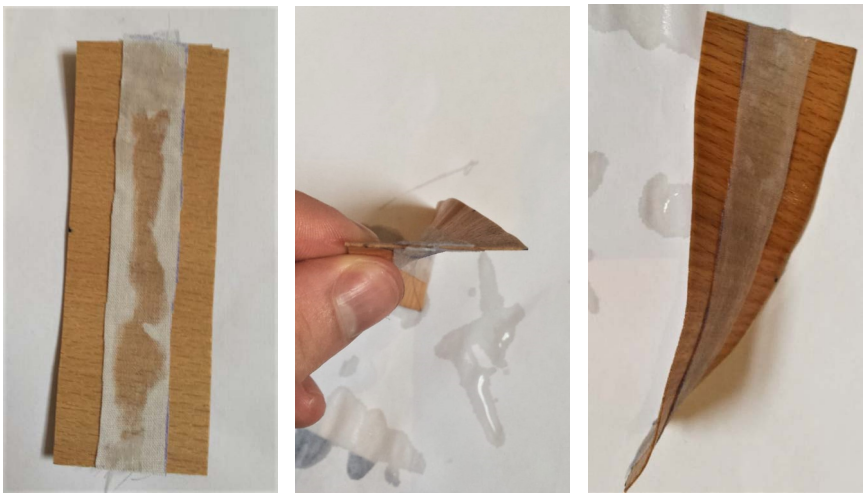

(a) Dry, undeformed state, front view. The cloth was applied with glue. It completely soaks through the cloth at some locations.

(b) Wet, deformed state, top view. The geometry is rotatet to an angle of almost 90 degrees.

(c) Wet, deformed state, front view. The centreline of the shell did not maintain its straight shape, the geometry bended sideways.

Figure A.1: Prototype consisting of a single slice of veneer, with attached cloth on both sides to restrict the centreline from elongation.

A.2.2. Veneer and PLA Clamps

In order to keep the additional shells in place and maintain a plus-shape during deformation, PLA clamps were printed directly onto the base. The veneer slices were then glued into place, embedded in the PLA clamps and base (see figure A.3). The clamps kept the shells together, maintaining the plus shape (figure A.3b). The centreline also stayed vertical during deformation. The resulting rotation was rather low however. This was caused by the additional stiffness of the plastic clamps, and by the absence of the constraint on the top edge.

A.3. Final Prototype

A.3.1. Design

Considering the advantages and disadvantages of the early versions of the prototypes, it was concluded that a centreline constraint is needed that has a good bonding with the shell, but does not add too much stiffness. After some experimentation, it was found that a thin rod of wood with its fibres oriented vertically provides the desired restriction of elongation, without adding too much stiffness to the system. The bond of wood on wood maintained its integrity during almost all the large deformations. See figure A.4 for version D of the final prototype, in dry and wet state.

A.3.2. Fabrication

In order to fabricate the shells as precise as possible, moulds were 3D printed corresponding to the dimensions of the five geometries A to E (table 1). A scalpel was used to cut the veneer without damaging the edges. Similarly, narrow wooden rods were cut. Cherry wood was chosen to be used for these rods, since it provided a nice contrasting colour.
An additional set of moulds was used to position the cherry rods exactly in the center of the shell. Once glued in place, The shells and rods were glued into two PLA clamps (see figure A.5 a and b) to satisfy constraint 2. These clamps contained a horizontal slit to envelop the shell, with a little notch to accommodate for the cherry slices on either end. Glue was applied inside the slit, after which the shell was pressed in. Additional braces were used to support the structure while the glue dried.

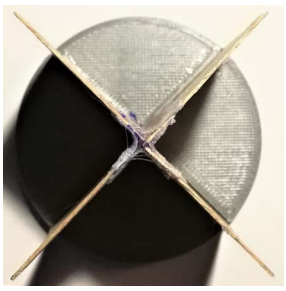

(a) Dry, undeformed state, top view.

(b) Wet, deformed state, top view. Notice the delamination of the cloth, resulting in misalignment of the shells.

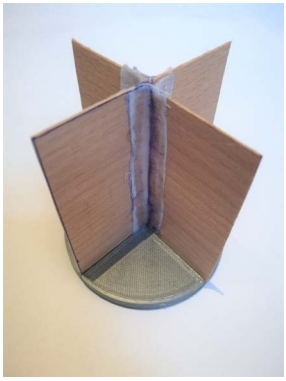

(c) Dry, undeformed state, front view. The four shells are held together using cloth.

(d) Wet, deformed state, front view. Notice the wrinkling of the outer edges of the shell.

Figure A.2: Prototype consisting of four slices of veneer placed in a PLA holder. The shells were joined together by glueing cloth along the centreline of the geometry.

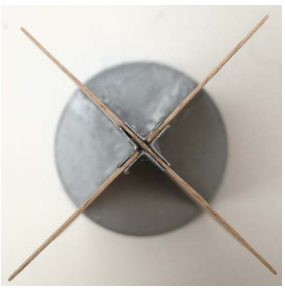

(a) Dry, undeformed state, top view.

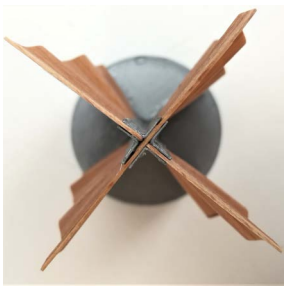

(b) Wet, deformed state, top view. Less misalignment of the shells happens.

(c) Dry, undeformed state, front view. The PLA brackets are printed directly on the PLA base.

(d) Wet, deformed state, front view.

Figure A.3: Prototype consisting of four slices of veneer placed in a PLA holder. The shells were joined together by gluing them inside PLA brackets, positioned along the centreline of the geometry.

A.4. Alternative Methods

A.4.1. Additive Manufacturing

Due to its form freedom, Additive Manufacturing (AM) was investigated as promising production method for the HRA. This form freedom would allow spatially curved surfaces like initial twist (see chapter 3.2) to be implemented in the design. Furthermore, it would remove the need of additional material near the shell centreline, since shells could be joined together via the additive manufacturing process. Finally, it adds the possibility of attaching connection interfaces directly to the actuated geometry.

Additive manufacturing of hygromorphic actuators has proven to be possible [34], hygromorphic bilayers fabricated with a standard 3D-printer exist [35]. In these designs, Fused Deposition Modelling (FDM) is used to add a thin layer of hygro-active filament to a non hygro-active support sheet. This hygro-active filament is a standard FDM filament (PLA) laced with approximately 20% wood fibres. During extrusion through the 3d-printer nozzle, these fibers align themselves with the extrusion direction [36, 37]. When exposed to water, the printed geometry only extends perpendicular to the fiber. By precisely controlling the extrusion direction [34, 38], the direction of hygroscopic expansion can be programmed into the geometry.

These principles have been tried on the presented design of the HRA. Each shell was modelled to have the same thickness as the nozzle diameter. Due to the layer-by-layer process of FDM-printing, this ensured that the orientation of the printed shell would correspond to a vertical hygroscopic elongation.

The centreline constraint was implemented by embedding a thin metal wire in the geometry. The bottom constraint was realised by printing a thicker base construction. For the purpose of this test, the top constraint was left out. The printed geometries can be seen in figure A.6.

Unfortunately, none of the 3D-printed structures showed deformation after being exposed to water, even after extended experimentation with filament and printer settings. This is most likely due to the thickness of

(a) Dry, undeformed state (geometry D).

(b) Wet, deformed state (geometry D).

Figure A.4: Final iteration of the prototypes, version geometry D. Notice the darker wood, functioning as the centreline constraint. The bond between the darker wood and the shell stayed intact even during the large rotation.

(a) Top part constraining the veneer and connecting the HRA to the torsion machine.

(b) Bottom part constraining the veneer and connecting the HRA to the torsion machine.

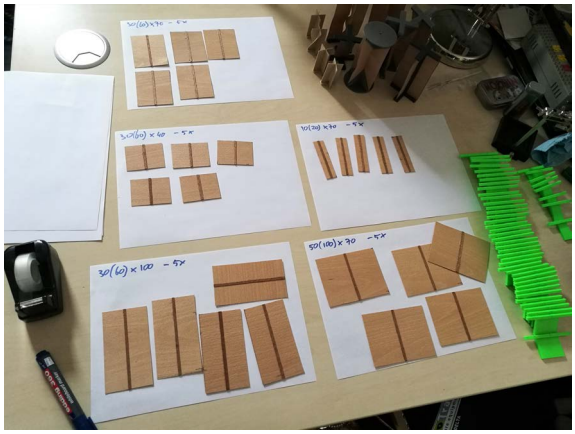

(c) Different geometries during the process of attaching the centreline constraint. On the right, the green braces can be seen.

Figure A.5: Different stages of the production process.

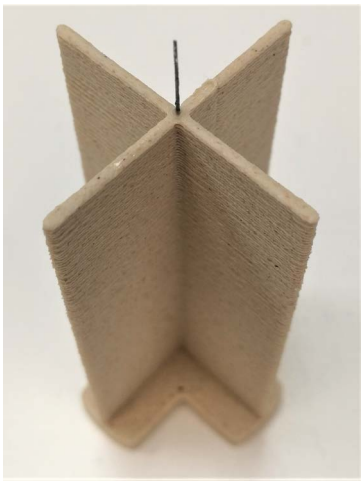

(a) Regular 3D-printed geometry in dry, undeformed state, front view.

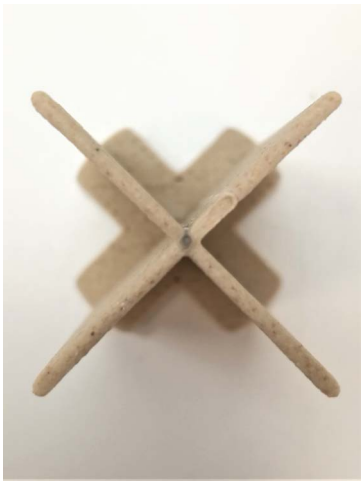

(b) Regular 3D-printed geometry in dry, undeformed state, top view.

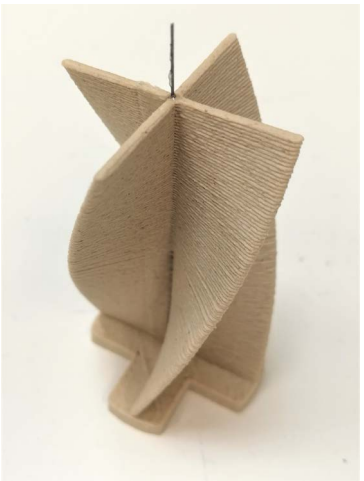

(c) 3D-printed geometry with initial twist in dry, undeformed state, front view.

Figure A.6: 3D-printed versions of the HRA in dry and undeformed state. None of them showed any deformation when being exposed to water. The shells have a thickness of exactly one nozzle diameter. Note the horizontal layers, resulting from the layer-by-layer process.

the printed shells. This thickness is limited by the nozzle diameter. One of the requirements for printing with wood filaments is the use of a larger nozzle, 0.6 mm compared to 0.4 mm for regular filament. The printed bilayer actuators from previous research are oriented with their shell parallel to the horizontal plane, so its thickness can be determined by the layer height [34, 35]. This can be as small as 0.2 mm, resulting in a thinner shell that is better capable of absorbing water.
Nevertheless, the aforementioned advantages of additive manufacturing could benefit the design of the HRA. Further investigation could be done to adapt the process to work for the presented actuator design.

A.4.2. Other Alternatives

During the prototype design process, various other manufacturing methods of hygromorphic materials were found. Most of them were still in their experimental phase and were therefore not considered for the fabrication of the prototypes. They are gathered here together with the earlier discussed methods, to provide a starting point for the reader if investigation of other manufacturing possibilities is desired.

1. Using existing materials
    (a) Wood
        i. Large wooden structures [23, 39]
        ii. Veneer (appendix A.2 and appendix B)
    (b) Natural fibre sheets (e.g. cottonid [40])
2. Using custom materials
    (a) Composite swelling polymers
        i. with embedded artificial fibres [20, 41]
        ii. with embedded natural fibres [42, 43]
            A. Additive Manufacturing (appendix A.4.1)
    (b) Non-composite swelling polymers [44–46]
        i. Hydrogels [47]
        ii. Liquid crystals [48]
        iii. Surface-patterned films [49]

B

Determining material properties

To be able to compare the results of the numerical simulations with the observed behaviour of the fabricated prototypes, the material model implemented in the simulations needed to resemble the material that the prototypes are made of. How these properties were determined, is described in this chapter.

B.1. Elongation due to Hygroscopic Expansion

The elongation of beech veneer was determined by cutting out slices and submerging them in water for at least ten minutes. The length and width of the slices were precisely measured using a calliper. These measurements were then used to calculate the hygroscopic Engineering and Lagrange strains, for use in the analytical model and the numerical calculations, respectively. Table B.1 provides an overview of the dimensions and the resulting engineering strain, being 0 parallel to the fibre (u-direction of the shell) and 0.084 perpendicular to the fibre (v-direction of the shell). The Lagrange strain was determined in a similar way, resulting in 0 parallel and 0.088 perpendicular to the fibre.

	Dry		Wet		Difference		Engineering Strain	
#	Length (mm)	Width (mm)	Length (mm)	Width (mm)	Length (mm)	Width (mm)	S_T (-)	S_L (-)
1	50.1	29.8	54.1	29.8	4.0	0	0.08	0
2	50.4	29.9	54.5	29.9	4.0	0	0.08	0
3	50.4	29.9	54.8	29.9	4.4	0	0.09	0
4	50.1	30.1	54.7	30.1	4.6	0	0.09	0
5	49.8	29.9	53.9	29.9	4.1	0	0.08	0
						Mean	0.084	0

Table B.1: Dimensions of the five specimen and their resulting engineering strain when exposed to water.

B.2. Young's Moduli

To determine the Young's modulus of the wood, three-point bending tests were performed on wet and dry specimen of veneer. A simple setup was build on a scale. Two bars with a thickness W_0 of 6.6 mm were taped on the plateau of the scale to form a span of 65 mm. Specimen were placed on the bars and pressed downwards until they touched the plateau of the scale, while reading the mass M shown on the display. This mass was converted in weight P, and together with the moment of inertia I, the Young's moduli could be calculated. The test setup and a schematic showing relevant dimensions is depicted in figures B.1 a and b. The dimensions of the specimen are shown in table B.2.

Due to the orthotropic nature of wood, measurements were done in two orientations. Orientation A, which measures the Young's modulus perpendicular to the fibre direction (E_T); and Orientation B, which measures the Young's modulus parallel to the fibre direction (E_L). Five specimen were measured this way, each of them in two states (wet and dry). This resulted in a total of 20 measurements. Mean values were calculated for each orientation in each state. Table B.2 shows the results of the measurements, table B.3 contains the mean values.

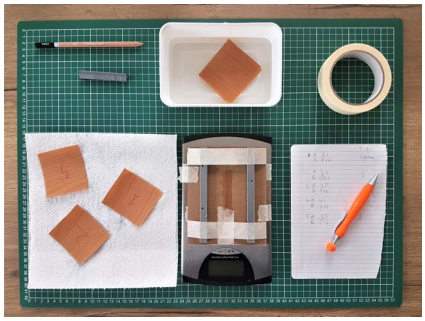

(a) Materials used during the test. Specimen were placed on the scale in dry and in wet state and manually deformed, using the display to determine the load at maximum deformation.

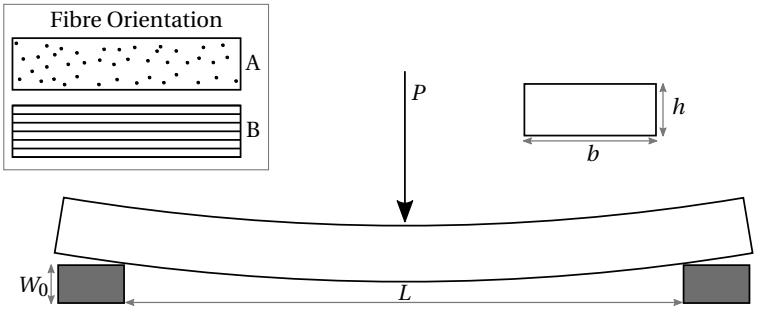

(b) Schematic of the test setup, showing all relevant dimensions.

Figure B.1: Overview of the test setup of the three-point bending test.

#	Specimen Orientation	State	Dimensions L (mm)	b (mm)	h (mm)	I (mm^4)	W_0 (mm)	Load M (kg)	P (N)	Young's Modulus E (N/mm^2)	
1	A	dry	60	65.0	0.62	1.291	6.6	0.041	0.402	E_T	212.43
		wet						0.032	0.314		165.80
	B	dry		65.4		1.299		1.080	10.595	E_L	5561.47
		wet						0.730	7.161		3759.14
2	A	dry	60	65.5	0.62	1.301	6.6	0.039	0.383	E_T	200.52
		wet						0.031	0.304		159.39
	B	dry		65.1		1.293		1.099	10.781	E_L	5685.39
		wet						0.870	8.535		4500.72
3	A	dry	60	64.4	0.62	1.279	6.6	0.038	0,37278	E_T	198.72
		wet						0.037	0.363		193.49
	B	dry		65.8		1.306		1.113	10.919	E_L	5696.56
		wet						0.890	8.731		4555.20
4	A	dry	60	64.8	0.62	1.287	6.6	0.040	0.392	E_T	207.87
		wet						0.035	0.343		181.90
	B	dry		65.3		1.297		1.120	10.987	E_L	5776.28
		wet						0.850	8.339		4383.79
5	A	dry	60	65.3	0.62	1.297	6.6	0.042	0.412	E_T	216.61
		wet						0.033	0.324		170.19
	B	dry		64.5		1.281		1.030	10.104	E_L	5378.01
		wet						0.890	8.731		4647.01

Table B.2: Overview of measurements used to perform the three-point bending test to determine the Young's moduli of the veneer.

	Young's Modulus E_L (MPa)	E_T (MPa)
Dry	5619.54	207.23
Wet	4369.17	174.16

Table B.3: Mean values of the Young's moduli parallel and perpendicular to the grain of the veneer, resulting from the measurements shown in table B.2

C

Description of test setup

C.1. Measuring Rotation

Two different test setups were used to analyze the performance of the HRA. First, the rotation of the wet and deformed geometry was measured by placing a camera directly above the geometry. This camera was linked to a laptop running the image analysis software ImageJ [29]. Reference features were present on both the test setup and the geometry. These features could be used as anchor points for angle measurement in ImageJ. See image C.1 for an overview of the setup.

(a) Overview of the angle measurement setup. The grey plateau is used to support a mobile phone, providing the camerafeed to ImageJ.

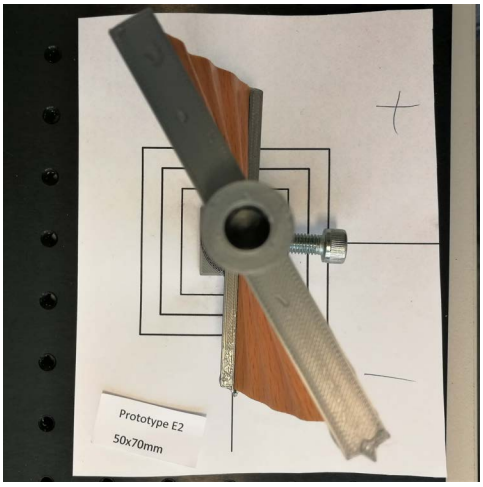

(b) Image of rotated prototype as seen by the camera. These images were fed to ImageJ so that the angle could be measured.

Figure C.1: Various aspects of the setup with which the angle measurements were performed. Note the black lines on the test set-up (figure a) and the protruding triangles on the specimen(figure b); these features were used as anchor points for the angle measurement in ImageJ.

C.2. Measuring Torque

Torque measurements were performed by rotating the specimen using a Zwick Z005 while measuring the torque with an HBM T20WN torque meter. The printed clamps that were used to built the prototypes were connected directly to the static and actuated ends of the machine (figures C.2 a and b). First, the top part of the geometry was connected to the upper part of the machine. This upper part was then translated downward so that the bottom part could also be connected, making sure not to crush the specimen.
Once connected, the current position and orientation was saved as neutral point of the machine, enabling all further movements to be implemented from this position. A stepwise rotation as outlined in (section II-F of

chapter 2) was imposed on the geometry, while measuring the torque output with a loadcell positioned at the bottom receiver of the machine.
Figure C.2c shows the full setup of a specimen connected to the torsion machine before rotation. Figure C.2b shows a closeup of a clamped specimen after the imposed rotation.

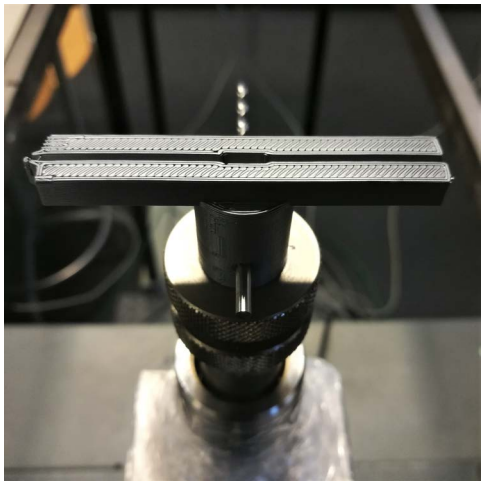

(a) Empty PLA part connected to the lower static part of the torsion machine.

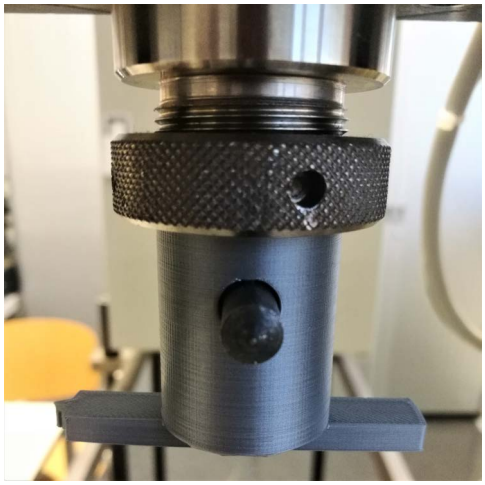

(b) Empty PLA part connected to the upper actuated part of the torsion machine.

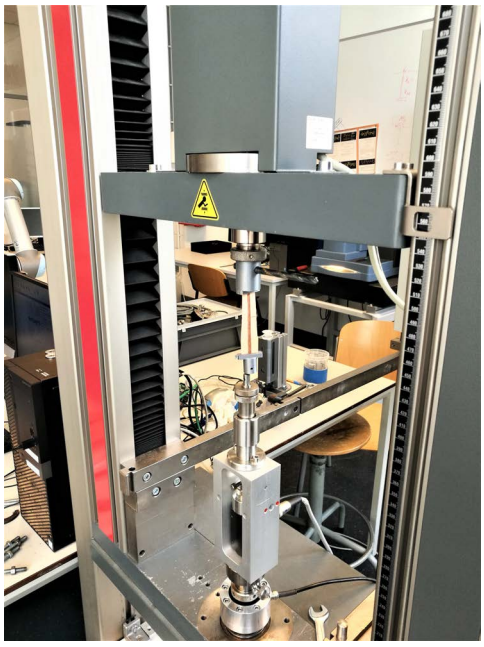

(c) Overview of the torsion-machine with attached specimen. Photo taken during the positioning phase; the specimen is disconnected at the bottom.

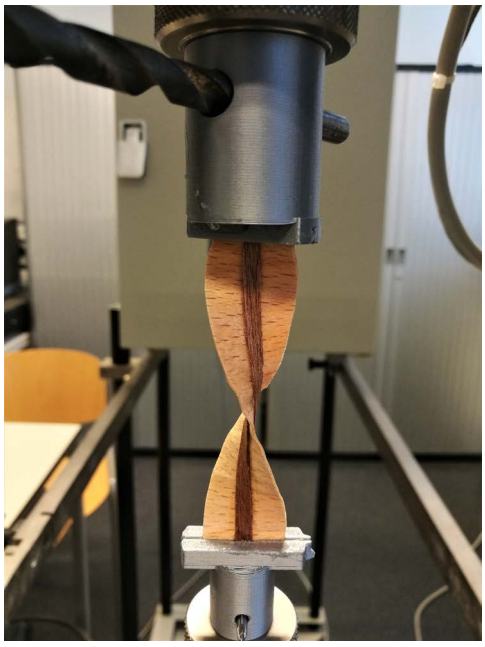

(d) Closeup of a specimen connected to the torsion machine.

Figure C.2: Various aspects of the torsion machine and connection interfaces with which the torsion tests were performed.

D

Numerical Simulation

As stated in section II-C of chapter 2, the numerical simulation is performed using an Isogeometric Analysis package (IGA) to construct and analyse the shell [25]. The simulation consists of two parts. First, many different geometries are deformed using a Lagrange strain to simulate hygroscopic elongation and subsequent morphing of the geometry. Second, some key deformed geometries were subjected to a rotation around the z-axis while measuring the torque. The following sections will describe each part in more detail, an overview of the complete simulation setup is given in figure D.1.

D.1. Hygromorphing - Regular Solver

An initial shell (Geometry A) of 30 by 70 by 0.62 millimetre is constructed. This shell is build as a NURBS-surface with 10 control points in u-direction (initially horizontal direction) and 100 points in v-direction (initially vertical direction), resulting in a total of 1000 control points or nodes. The bottom and top node of the centreline are defined as 'clamping points'; they can be used to apply or measure displacements, forces or moments. An orthotropic material model is implemented, with properties as specified in tables B.1 and B.2. Each node is given an initial vertical Lagrange strain.
Constraints are implemented on the surface to realise the restrictions as outlined in chapter II-A. Nodes along the bottom edge are completely fixed, realising a clamping-constraint. Nodes along the top edge can only translate in the xy-plane and are not allowed to rotate. They are also rigidly connected to their neighbours. Finally, the nodes on the centreline have their translations fixed and their rotations free, to simulate the symmetry across the z-axis. See figure 4b of chapter 2 for a simplified representation of the model.
In order to help the solver overcome buckling, and to try to come up with a solution near the maximum achievable angle, an initial small moment is applied to the upper clamping point. additionally, a small initial disturbance and small initial twist are implemented to force the geometry to always deform anti-clockwise. These steps are removed before the post-processing. With this completed model, the solving step can be started.
The amount of strain implemented on the nodes is incrementally increased each time step, being zero at t_{start} and maximum at t_{end}. Each step, the solver iterates to minimize the amount of energy in the shell. When the conversion threshold is reached, the solver moves on to the next step, with a higher strain and therefore a higher deformation.
When all steps are completed and the maximum hygroscopic strain is implemented, some post-processing is done to determine aspects like the resulting angle (figures 2.7, 2.8, 3.1a and 3.3a) and engineering strain per percentage of radius (figures 2.9 and 3.1b). This data is saved as a dataset, together with the deformed geometry and its material model.

D.2. Hygromorphing - Solving from Previously Solved Geometry

Because of the computation time and the convergence difficulties of the regular solving method, a different approach is implemented to get a large amount of deformed geometries.
Geometry A is taken as central geometry; its dataset is loaded. The parameter of interest is slightly increased and a new undeformed geometry is build. The deformation of the old geometry is taken and projected onto

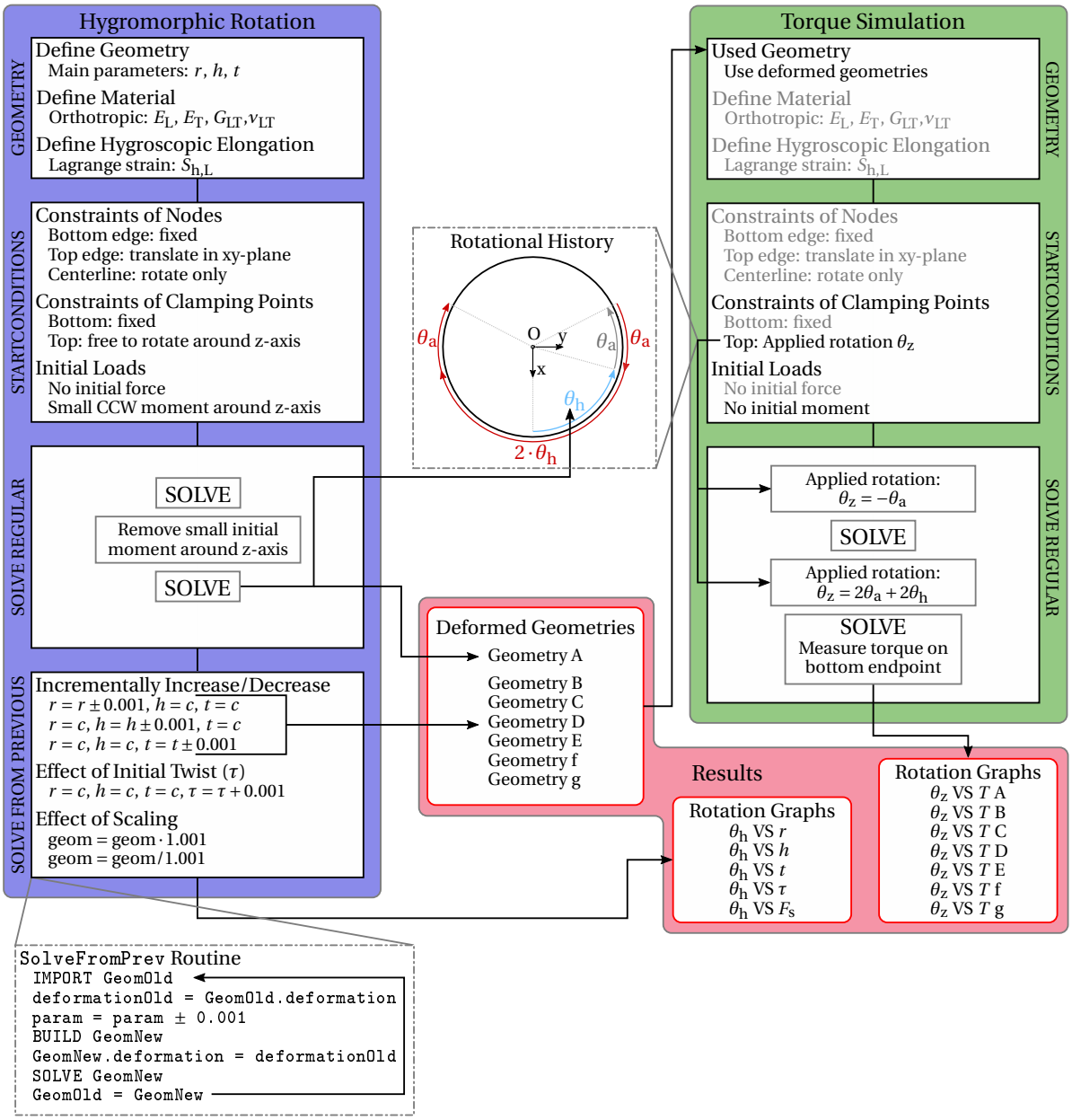

Figure D.1: Overview of the steps for each of the two parts of the simulation. The blue path depicts the steps taken to hygroscopically deform the geometries. The green path depicts the steps for the torque simulations. Finally, the red section shows the resulting data and graphs, and where they originate from. The two insets give more explanation about the `SolveFromPrev` routine of the hygromorphing and the rotational history of the geometry used in the torque simulations.

the undeformed new geometry. Because of the difference between the new and old geometry, this new deformed geometry will have an error. The new deformed geometry is processed by the solver again. Since the difference between the old deformed geometry and the new deformed geometry is very small, it is easy for the solver to converge to the new deformed geometry, correcting the small mistake.

The new deformed geometry is put through the same post-processing steps as implemented in the regular solving method, after which it is saved as a dataset. This dataset is then loaded again as the old deformed geometry and the whole process begins anew. See the inset on the bottom left of figure D.1, explaining the `SolveFromPrev` routine in pseudo-code.

The advantage of solving geometries this way, is that for each parameter of interest, many different geometries can be created bidirectionally from the central geometry A. This enabled the plotting of near-continuous line segments in the graphs depicting parameter vs resulting angle. It further provides a big database of deformed geometries, from which individual geometries can be selected for torque simulations. This is exactly

the way the remaining geometries are created. Geometries B and C result from stepwise increasing and decreasing height h while keeping the remaining parameters constant. Likewise, Geometries D and E result from varying radius r, geometries f and g result from varying thickness t and geometries h, i, j result from varying initial twist τ. See table E.1 for an overview of the specific geometries and their dimensions.

D.3. Torque Simulation

Each of the datasets of the seven deformed geometries A to g is subsequently loaded and subjected to torque simulations. First, an additional anti-clockwise rotation θ_a is applied on the upper clamping point and the solver is started. After completion, a clockwise rotation of $2\theta_a + 2\theta_h$ is applied and the solver is started again, this time while measuring the torque on the bottom clamping point. These two solver steps are performed using minimal energy as convergence criterion.
The measured torque for each time step is saved in a dataset, together with the rotated geometry. This torque is then used to form the angle-torque graphs in this thesis.
Rotating the geometries by means of actuating the upper clamping point proved difficult at times. A lot of experimentation had to be done to complete the torque simulations of the seven deformed geometries presented in this thesis. Amount of simulation steps, size of θ_a and stiffness of the clamping constraints had to be tweaked for each geometry. The extensive amount of work this took made it difficult to solve much more torque simulations.
To remedy this, a similar routine could be implemented as the `SolveFromPrev` routine of the hygromorphic deformation. This would be a bit more complicated, since during the torque tests the intermediate steps are also of interest, while during the hygromorphic deformation only the end-state is solved.

E

Supplementary info

Dimensions of Geometries

Table of all geometries used in the text

Version	Radius r (mm)	Height h (mm)	Thickness t (mm)	Initial Twist τ (deg)
A	30	70	0.62	0
B	30	40	0.62	0
C	30	100	0.62	0
D	10	70	0.62	0
E	50	70	0.62	0
f	30	70	0.32	0
g	30	70	1.22	0
h	30	70	0.62	45
i	30	70	0.62	90
j	30	70	0.62	180

Table E.1: Dimensions of the geometries discussed in this thesis. The first seven geometries are treated in the paper in chapter 2. Versions denoted in capitals (A-E) were also produced and tested as prototypes.

Glossary

AM Additive Manufacturing

FDM Fused Deposition Modelling. Method of 3D printing that uses a hot nozzle to extrude material in a programmed shape.

HRA Hygromorphic Rotational Actuator

IGA Iso-Geometric Analysis

NURBS surface Non-Uniform Rational Basis Spline, the way surfaces are modelled in the Iso-Geometric Analysis

PLA Poly-Lactic Acid. Often used material in an FDM extrusion.

u-direction First of the principle directions of a B-spline surface. In the case of the HRA, this is the initially horizontal direction

v-direction Second of the principle directions of a B-spline surface. In the case of the HRA, this is the initially vertical direction

Acknowledgements

First and foremost, I would like to thank Heike and Giuseppe for their unceasing support during this project. Heike, your enthusiasm for every new result of this project was uplifting and your critical view made our meetings very fruitful. Giuseppe, for every problem I faced, you had at least two solutions. Your knowledge of and passion for compliant shell mechanisms is contagious, I am starting to find regular mechanisms boring. Thanks for mentoring me during my internship and my thesis, I really enjoyed it and I learned a lot.
To everyone at the shell-skeletons group, thanks for your feedback, your ideas, and your interesting projects. The world of compliant shell mechanisms is interesting and broad; you helped uncover a large part of it for me! Sjaak, thanks for proofreading my paper, your comments helped restructure it to its final form.

I also had a lot of help during the fabrication and testing of the prototypes. Thomas and Mischa, thanks for assisting me and letting me use your 3D-printers. I could not have made the prototypes without you! Patrick, your advice in the design of the experimental setup and the help during the tests was invaluable. To everyone at PME-labs, thanks for the quick additional printing and the flexibility of access to the faculty. It really helped keeping things on track in these weird times.

Thanks to the boys at FrameFlux to allow me to bring my engineering skills in practice. Yufe, thanks for proof-reading my paper and improving my English. Good luck on those Dutch courses!

I would also like to thank al my friends that I met during my studies here at TU Delft. Each of you made it an unforgettable time that has shaped me to who I am today.
To my friends in Flow, CRISP, Wakki, Brasszzinga and Haex Trio; thanks for continuing to write and perform new and exciting music with me. Music is really my favourite form of self-expression and I feel privileged to be able to do that in such a good company.
To Moos and Tobias, thanks for all those late night talks and adventures, and thanks for dragging me to the library each next morning. One day we will do that roadtrip, one day we will form that band!
To everyone at Groover, thanks for providing a platform where unique musical ideas could grow and flourish, effectively giving me an education in music next to my engineering studies. Also, thank you for providing the much needed late night jam sessions and parties. It really helped me regain energy after a long week of lectures.

Thanks to my parents, who supported me without hesitation during my long journey. They effectively enabled me to both pursue an education in engineering and work on my music at the same time, for which I am forever grateful.
Thanks to Thomas, Annelieke and Martijn for making my early life so enjoyable. Let's go and annoy our parents a bit more when this lockdown is over!
To Oom Jaap and Opa Chris, I am very grateful that you planted the scientific seed at an early age. As fellow TU Delft alumni, I'll hope I make you proud.

Finally, Sam, thanks for bearing with me all these years. You have the rare ability to cheer me up when I am down, and to motivate me when I have absolutely no discipline to be productive. I could not have done this without you!

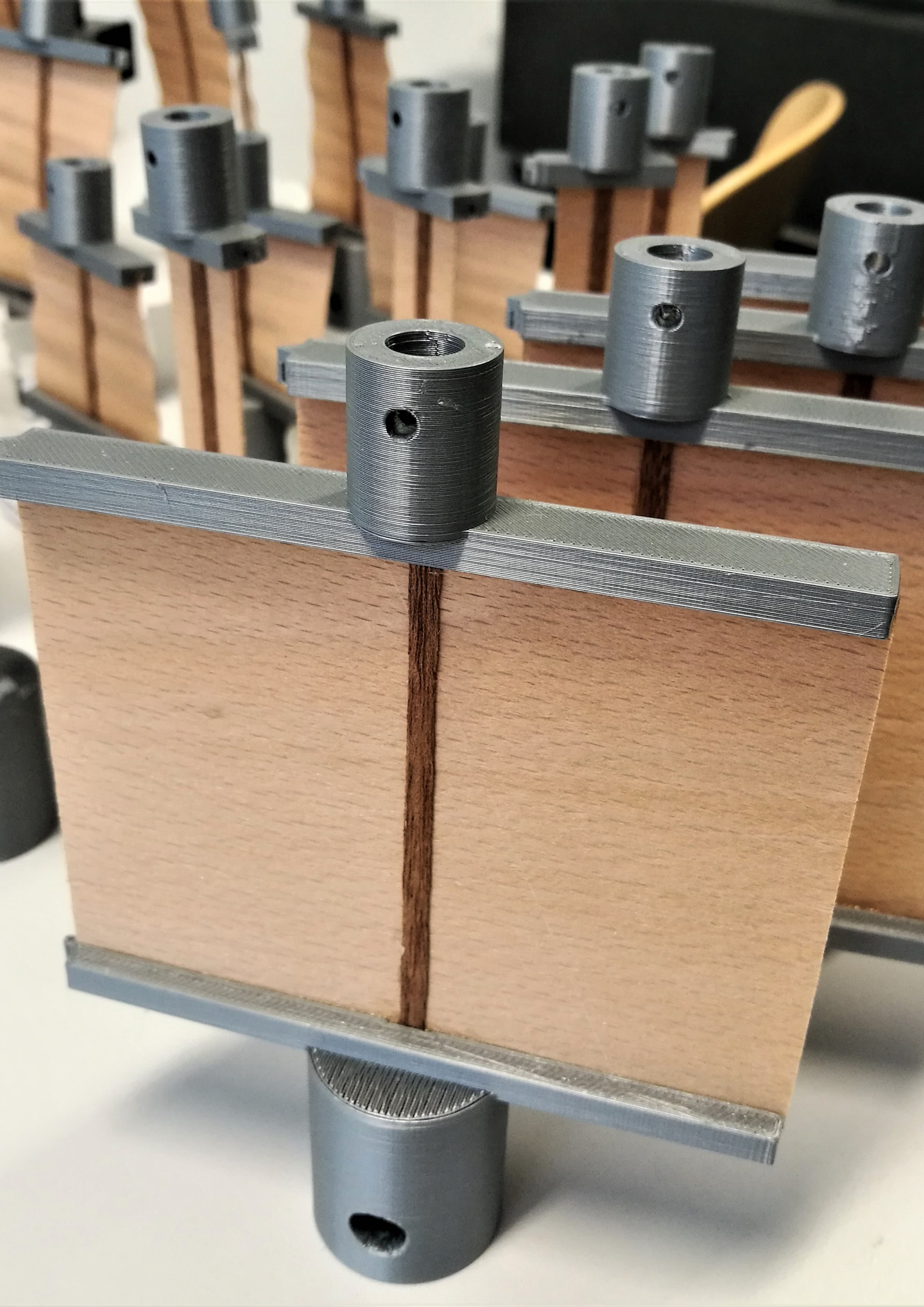

Bibliography

[1] A. Sakes, M. D. Van Wiel, P. W. Henselmans, J. L. Van Leeuwen, D. Dodou, and P. Breedveld, "Shooting mechanisms in nature: A systematic review," *PLoS ONE*, vol. 11, no. 7, pp. 1–46, 2016.

[2] R. Elbaum, L. Zaltzman, I. Burgert, and P. Fratzl, "The role of wheat awns in the seed dispersal unit," *Science*, vol. 316, no. 5826, pp. 884–886, 2007.

[3] S. Joosten, G. Radaelli, and H. Vallery, "Compliant Shell Deformation in Plants : A Designer's Toolbox," tech. rep., Delft University of Technology, 2019.

[4] J. Dumais and Y. Forterre, "Vegetable Dynamicks: The Role of Water in Plant Movements," *Annual Review of Fluid Mechanics*, vol. 44, no. 1, pp. 453–478, 2011.

[5] V. Charpentier, P. Hannequart, S. Adriaenssens, O. Baverel, E. Viglino, and S. Eisenman, "Kinematic amplification strategies in plants and engineering," *Smart Materials and Structures*, vol. 26, no. 6, pp. 63002 – 63002, 2017.

[6] R. Elbaum, "Structural Principles in the Design of Hygroscopically Moving Plant Cells," in *Plant Biomechanics: From Structure to Function at Multiple Scales* (A. Geitmann and J. Gril, eds.), pp. 235–245, Sainte-Anne-de-Bellevue, QC: Springer International Publishing, 2018.

[7] E. Reyssat and L. Mahadevan, "Hygromorphs: From pine cones to biomimetic bilayers," *Journal of the Royal Society Interface*, vol. 6, no. 39, pp. 951–957, 2009.

[8] M. Hayashi, S. P. Gerry, and D. J. Ellerby, "The seed dispersal catapult of Cardamine parviflora (Brassicaceae) is efficient but unreliable," *American Journal of Botany*, vol. 97, no. 10, pp. 1595–1601, 2010.

[9] H. Liang and L. Mahadevan, "Growth, geometry, and mechanics of a blooming lily," *Proceedings of the National Academy of Sciences*, vol. 108, no. 14, pp. 5516–5521, 2011.

[10] H. Kobayashi, B. Kresling, and J. F. Vincent, "The geometry of unfolding tree leaves," *Proceedings of the Royal Society B: Biological Sciences*, vol. 265, no. 1391, pp. 147–154, 1998.

[11] T. Speck, G. Bold, T. Masselter, S. Poppinga, S. Schmier, M. Thielen, and O. Speck, "Biomechanics and Functional Morphology of Plants - Inspiration for Biomimetic Materials and Structures," in *Plant Biomechanics: From Structure to Function at Multiple Scales* (A. Geitmann and J. Gril, eds.), ch. 4, pp. 399 – 433, Cham: Springer International Publishing, 1 ed., 2018.

[12] S. Schleicher, J. Lienhard, S. Poppinga, T. Speck, and J. Knippers, "A methodology for transferring principles of plant movements to elastic systems in architecture," *CAD Computer Aided Design*, vol. 60, pp. 105–117, 2015.

[13] S. Poppinga, C. Zollfrank, O. Prucker, J. Rühe, A. Menges, T. Cheng, and T. Speck, "Toward a New Generation of Smart Biomimetic Actuators for Architecture," *Advanced Materials*, vol. 30, no. 19, pp. 1–10, 2018.

[14] I. Burgert and P. Fratzl, "Actuation systems in Plants as prototypes for bioinspired devices," *Philosophical Transactions of the Royal Society A: Mathematical, Physical and Engineering Sciences*, vol. 367, no. 1893, pp. 1541–1557, 2009.

[15] M. Rüggeberg and I. Burgert, "Bio-Inspired wooden actuators for large scale applications," *PLoS ONE*, vol. 10, no. 4, pp. 1–16, 2015.

[16] L. Zhang, S. Chizhik, Y. Wen, and P. Naumov, "Directed Motility of Hygroresponsive Biomimetic Actuators," *Advanced Functional Materials*, vol. 26, no. 7, pp. 1040–1053, 2016.

[17] K. M. Al-Obaidi, M. Azzam Ismail, H. Hussein, and A. M. Abdul Rahman, "Biomimetic building skins: An adaptive approach," *Renewable and Sustainable Energy Reviews*, vol. 79, no. May, pp. 1472–1491, 2017.

[18] D. M. Wood, D. Correa, O. D. Krieg, and A. Menges, "Material computation-4D timber construction: Towards building-scale hygroscopic actuated, self-constructing timber surfaces," *International Journal of Architectural Computing*, vol. 14, no. 1, pp. 49–62, 2016.

[19] S. Reichert, A. Menges, and D. Correa, "Meteorosensitive architecture: Biomimetic building skins based on materially embedded and hygroscopically enabled responsiveness," *CAD Computer Aided Design*, vol. 60, pp. 50–69, 2015.

[20] B. Shin, J. Ha, M. Lee, K. Park, G. H. Park, T. H. Choi, K. J. Cho, and H. Y. Kim, "Hygrobot: A self-locomotive ratcheted actuator powered by environmental humidity," *Science Robotics*, vol. 3, no. 14, pp. 1–9, 2018.

[21] D. Raviv, W. Zhao, C. McKnelly, A. Papadopoulou, A. Kadambi, B. Shi, S. Hirsch, D. Dikovsky, M. Zyracki, C. Olguin, R. Raskar, and S. Tibbits, "Active printed materials for complex self-evolving deformations," *Scientific Reports*, vol. 4, no. 7422, pp. 1–8, 2014.

[22] R. M. Erb, J. S. Sander, R. Grisch, and A. R. Studart, "Self-shaping composites with programmable bioinspired microstructures," *Nature Communications*, vol. 4, pp. 1–8, 2013.

[23] David E. Kretschmann, "Mechanical Properties of Wood," in *Wood Handbook - Wood as an Engineering Material* (R. J. Ross, ed.), ch. 5, pp. 5–1 – 5–45, Madison, WI: U.S. Dept. of Agriculture, Forest Service, Forest Products Laboratory, centennial ed., 2010.

[24] H. Steinhaus, "Squirels, Screws, Candles, Tunes, and Shadows," in *Mathematical Snapshots*, pp. 229–230, Mineola, New York: Dover Publications, Inc., third ed., 1983.

[25] A. P. Nagy, *Isogeometric Design Optimisation*. PhD thesis, Delft University of Technology, 2011.

[26] S. Hering, D. Keunecke, and P. Niemz, "Moisture-dependent orthotropic elasticity of beech wood," *Wood Science and Technology*, vol. 46, no. 5, pp. 927–938, 2012.

[27] P. Niemz, T. Ozyhar, S. Hering, and W. Sonderegger, "Moisture Dependent Physical-Mechanical Properties from Beech Wood in the Main Directions," *Pro Ligno*, vol. 11, no. 4, pp. 37–42, 2015.

[28] E. Güntekin, T. Y. Aydin, and P. Niemz, "Some orthotropic elastic properties of fagus orientalis as influenced by moisture content," *Wood Research*, vol. 61, no. 1, pp. 95–104, 2016.

[29] C. A. Schneider, W. S. Rasband, and K. W. Eliceiri, "NIH Image to ImageJ: 25 years of image analysis," *Nature Methods*, vol. 9, no. 7, pp. 671–675, 2012.

[30] K. A. Seffen, "Hierarchical multi-stable shapes in mechanical memory metal," *Scripta Materialia*, vol. 56, no. 5, pp. 417–420, 2007.

[31] J. P. Udani and A. F. Arrieta, "Analytical Modeling of Multi-sectioned Bi-stable Composites: Stiffness Variability and Embeddability," *Composite Structures*, vol. 216, no. February, pp. 228–239, 2019.

[32] H. Yang and L. Ma, "1D to 3D multi-stable architected materials with zero Poisson's ratio and controllable thermal expansion," *Materials and Design*, vol. 188, pp. 1–16, 2020.

[33] A. F. Arrieta, V. Van Gemmeren, A. J. Anderson, and P. M. Weaver, "Dynamics and control of twisting bi-stable structures," *Smart Materials and Structures*, vol. 27, no. 2, 2018.

[34] A. L. Duigou, M. Castro, R. Bevan, and N. Martin, "3D printing of wood fibre biocomposites: From mechanical to actuation functionality," *Materials and Design*, vol. 96, pp. 106–114, 2016.

[35] D. Correa, A. Papadopoulou, C. Guberan, N. Jhaveri, S. Reichert, A. Menges, and S. Tibbits, "3D-Printed Wood: Programming Hygroscopic Material Transformations," *3D Printing and Additive Manufacturing*, vol. 2, no. 3, pp. 106–116, 2015.

[36] B. G. Compton and J. A. Lewis, "3D-printing of lightweight cellular composites," *Advanced Materials*, vol. 26, no. 34, pp. 5930–5935, 2014.

[37] A. Sydney Gladman, E. A. Matsumoto, R. G. Nuzzo, L. Mahadevan, and J. A. Lewis, “Biomimetic 4D printing,” *Nature Materials*, vol. 15, no. 4, pp. 413–418, 2016.

[38] T. Van Manen, S. Janbaz, and A. A. Zadpoor, “Programming 2D/3D shape-shifting with hobbyist 3D printers,” *Materials Horizons*, vol. 4, no. 6, pp. 1064–1069, 2017.

[39] D. Wood, C. Vailati, A. Menges, and M. Rüggeberg, “Hygroscopically actuated wood elements for weather responsive and self-forming building parts – Facilitating upscaling and complex shape changes,” *Construction and Building Materials*, vol. 165, pp. 782–791, 2018.

[40] R. Scholz, M. Langhansl, C. Zollfrank, and F. Walther, “Experimental study on the actuation and fatigue behavior of the biopolymeric material Cottonid,” in *Materials Today: Proceedings*, vol. 7, pp. 476–483, Elsevier Ltd, 2019.

[41] A. Krauklis, A. Gagani, and A. Echtermeyer, “Prediction of Orthotropic Hygroscopic Swelling of Fiber-Reinforced Composites from Isotropic Swelling of Matrix Polymer,” *Journal of Composites Science*, vol. 3, no. 1, p. 10, 2019.

[42] A. Le Duigou and M. Castro, “Moisture-induced self-shaping flax-reinforced polypropylene biocomposite actuator,” *Industrial Crops and Products*, vol. 71, pp. 1–6, 2015.

[43] A. L. Duigou, S. Requile, and J. Beaugrand, “Natural fibres actuators for smart bio-inspired hygromorph biocomposites,” *Smart Materials and Structures*, vol. 26, no. 12, 2017.

[44] S. W. Lee, J. H. Prosser, P. K. Purohit, and D. Lee, “Bioinspired Hygromorphic Actuator Exhibiting Controlled Locomotion,” *ACS Macro Letters*, vol. 2, no. 11, pp. 960–965, 2013.

[45] Y. Liu, J. Genzer, and M. D. Dickey, “"2D or not 2D": Shape-programming polymer sheets,” *Progress in Polymer Science*, vol. 52, pp. 79–106, 2016.

[46] D. P. Holmes, M. Roché, T. Sinha, and H. A. Stone, “Bending and twisting of soft materials by non-homogenous swelling,” *Soft Matter*, vol. 7, no. 11, pp. 5188–5193, 2011.

[47] J. C. Athas, C. P. Nguyen, B. C. Zarket, A. Gargava, Z. Nie, and S. R. Raghavan, “Enzyme-Triggered Folding of Hydrogels: Toward a Mimic of the Venus Flytrap,” *ACS Applied Materials and Interfaces*, vol. 8, no. 29, pp. 19066–19074, 2016.

[48] L. T. De Haan, J. M. Verjans, D. J. Broer, C. W. Bastiaansen, and A. P. Schenning, “Humidity-responsive liquid crystalline polymer actuators with an asymmetry in the molecular trigger that bend, fold, and curl,” *Journal of the American Chemical Society*, vol. 136, no. 30, pp. 10585–10588, 2014.

[49] S. Liang, X. Qiu, J. Yuan, W. Huang, X. Du, and L. Zhang, “Multiresponsive Kinematics and Robotics of Surface-Patterned Polymer Film,” *ACS Applied Materials and Interfaces*, vol. 10, no. 22, pp. 19123–19132, 2018.